Applied Catalysis B: Environment and Energy 378 (2025) 125591

Contents lists available at ScienceDirect

Applied Catalysis B: Environment and Energy

journal homepage: www.elsevier.com/locate/apcatb

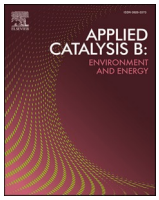

Selective production of market-valued dihydroxyacetone on two alloy phase surfaces by electrocatalytic oxidation of biomass-derived glycerol

Lee Seul Oh [a,1], Da Bean Han [b,1], Jechan Lee [c,1], So Hui Jeong [a], Ju Ye Kim [a], Youngmin Kim [d], Hyun Woo Kim [b,*], Hyung Ju Kim [a,*]

[a] Advanced Materials Division, Korea Research Institute of Chemical Technology (KRICT), 141 Gajeong-ro, Yuseong-gu, Daejeon 34114, Republic of Korea
[b] Department of Chemistry, Gwangju Institute of Science and Technology (GIST), 123 Cheomdangwagi-ro, Buk-gu, Gwangju 61005, Republic of Korea
[c] Department of Global Smart City & School of Civil, Architectural Engineering, and Landscape Architecture, Sungkyunkwan University (SKKU), 2066 Seobu-ro, Jangan-gu, Suwon-si, Gyeonggi-do 16419, Republic of Korea
[d] Chemical & Process Technology Division, Korea Research Institute of Chemical Technology (KRICT), 141 Gajeong-ro, Yuseong-gu, Daejeon 34114, Republic of Korea

ARTICLE INFO

Keywords:
Electrocatalytic glycerol oxidation
Selective dihydroxyacetone production
PtSb and $PtSb_2$ alloys
Hollow spherical electrocatalyst
DFT calculations
Oxidation reaction chemistry

ABSTRACT

Dihydroxyacetone (DHA) is recognized as a valuable chemical in cosmetic and pharmaceutical industries. Recently, electrocatalytic glycerol oxidation reaction (EGOR) technology has been attractive for selective DHA production. However, one fundamental question needs to be answered: Which catalytic active site affects the reaction chemistry and mechanism for the selective DHA production from EGOR. In this study, Pt-Sb hollow spherical electrocatalysts were prepared by a simple chemical synthesis method, which includes different catalytic phases, namely, PtSb and $PtSb_2$ alloys by controlling the Pt:Sb atomic ratio ($Pt_{8.64}Sb_{1.36}$, $Pt_{7.01}Sb_{2.99}$, and $Pt_{5.59}Sb_{4.41}$). Both experimental and computational methods were used to understand how and why the reaction performance and chemistry change with the PtSb and $PtSb_2$ alloy phases in the EGOR. The $Pt_{5.59}Sb_{4.41}$ electrocatalyst, which has a large portion of PtSb and $PtSb_2$ alloys, demonstrated superior EGOR activity over those of other ratios of Pt-Sb electrocatalysts, with a lower onset potential and higher Pt mass activity in the different pH conditions (acid, neutral, and base). Interestingly, in the EGOR, the $Pt_{5.59}Sb_{4.41}$ catalyst produced DHA with high selectivity of over 90 % in both acid and neutral conditions. The enhanced EGOR performances were related to the formed PtSb and $PtSb_2$ alloys at the surface structure of prepared Pt-Sb electrocatalysts. Density functional theory (DFT) calculations revealed that the Sb atoms changed the electronic properties of the Pt atoms and thus modulated the interaction between Pt atoms and adsorbates, which affected both the catalytic activity and DHA selectivity for the EGOR.

1. Introduction

Glycerol, a by-product of biodiesel, is generated by converting vegetable oils and animal fats into biodiesel; approximately 100 kg of glycerol is produced for every ton of biodiesel [1–4]. As biodiesel production has increased annually, the production of glycerol by-products has exceeded the demand. This has resulted in an oversupply of glycerol, which is expected to reach 4.0 billion kg per year by 2026 [4,5]. The price of glycerol has greatly decreased because of the oversupply of glycerol, making it commercially available in large quantities at low cost. The market prices of crude and refined glycerol are US$0.09–0.2 and US$0.6 per kg [6,7]. Therefore, how to efficiently convert glycerol into more value-added chemicals is still an ongoing project in the research communities.

Among the various conversion processes to produce valuable chemicals from glycerol, the electrocatalytic glycerol oxidation reaction (EGOR) has received attention as a promising technology that can produce value-added chemicals such as dihydroxyacetone (DHA, C3), lactic acid (LA, C3), glyceraldehyde (GAD, C3), glyceric acid (GLA, C3), tartronic acid (TTA, C3), oxalic acid (OXA, C2), glycolic acid (GCA, C2), and formic acid (FA, C1) by a selective glycerol oxidation reaction at the anode side and hydrogen by the hydrogen evolution reaction at the cathode side in an electrolytic cell. The hydrogen produced as a by-product at the cathode can be further utilized for hydrogenation

* Corresponding authors.
E-mail addresses: hwk@gist.ac.kr (H.W. Kim), hjkim@krict.re.kr (H.J. Kim).
[1] These authors are co-first authors who contributed equally to this work.

https://doi.org/10.1016/j.apcatb.2025.125591
Received 31 March 2025; Received in revised form 28 May 2025; Accepted 10 June 2025
Available online 11 June 2025

reactions to obtain more value-added chemicals [8–22]. This electrocatalytic conversion technology can be operated at ambient pressure and temperature without using any stoichiometric chemical oxidants such as O_2 and H_2O_2. Not using the chemical oxidants prevents overoxidation and thus the formation of unwanted by-products. By changing the electrode potential for the EGOR, it is possible to control the reaction kinetics and product selectivity [9,23,24]. Moreover, the electrocatalytic oxidation process of glycerol can be combined with renewable energy sources such as wind and solar, thereby establishing environmental and economic synergies. The simplicity of the electrocatalytic reactor design and reaction process has the potential to decrease the operating costs compared to conventional thermal catalytic reactor.

Precious metal-based catalysts such as Pt and Au have been extensively studied to oxidize glycerol at the anode in the EGOR because they have excellent electrocatalytic performance [25–34]. Pt and Au catalysts activate C-H and O-H bonds to generate C3 molecules such as GAD and GLA as the main products [25–29,31,32]. It has been reported that the Pt- and Au-based catalysts mainly produce GLA with high selectivity from the EGOR, which is further oxidized to GCA, TTA, OXA, and FA [27,32]. Experimental and techno-economic investigations have revealed that the GLA can be produced using the Pt catalyst with the minimum selling price (MSP) of $2.30 per kg of GLA for the EGOR process compared to $4.91 per kg of GLA for the non-electrocatalytic process [9]. Although the GLA is selectively produced from the EGOR, it has not been widely used in the market. This may be a limitation for the commercialization of the EGOR process. Therefore, strategies to produce more market-valued chemicals from the EGOR are required and should be considered in the research communities.

DHA, which can be produced by the EGOR, is a valuable chemical and is widely used in the cosmetic, pharmaceutical, fine chemical, and food industries [2,4,35,36]. DHA is produced by microbial fermentation of biomass-derived glycerol [37,38]. The annual production of DHA is at least 2000 tons, and the global market size of DHA is expected to grow steadily from USD 135.1 million in 2011 to USD 219.8 million by 2028, at a compound annual growth rate of about 5.59 % [38]. It is known that the price of DHA that is driven by substantial market demand is $150 per kg [35,36,39]. Thus, producing the market-valued DHA from the EGOR is a promising approach for the commercialization of this technology.

Recently, some catalytic materials have been tried and studied to produce DHA for the EGOR [40–59]. Pt catalysts combined with Bi and Sb demonstrated high selectivity of DHA for both electrocatalytic and non-electrocatalytic glycerol oxidations [8,14,40,41,43]. Some reports have claimed that it is possible to produce DHA selectively from the EGOR over Au-based catalysts [45,49,52]. In addition, non-precious metal-based oxides, such as CuO, CoO and MnO_2 catalysts have been tried to confirm the possibility of selective DHA production for the EGOR [48,50,51,53–55,57,58]. However, fundamental understanding of how we can control and change the selective DHA formation on the catalyst electrodes for the EGOR in different reaction environments and which specific catalytic active sites influence the EGOR activity and DHA selectivity has not yet been established. Thus, it is highly desirable to gain critical scientific insights on the reaction chemistry and mechanism through a systematic catalyst study for the selective DHA production from the EGOR.

Using both experimental and computational investigations, we performed a systematic study to understand on how the reaction performance and chemistry can be controlled for selective DHA production by the EGOR. In this work, using a simple one-pot chemical synthesis, we prepared Pt and Pt-Sb hollow structure electrocatalysts that had different catalytic phases, namely, PtSb and $PtSb_2$ alloys, by changing the Pt:Sb atomic ratio ($Pt_{8.64}Sb_{1.36}$, $Pt_{7.01}Sb_{2.99}$, and $Pt_{5.59}Sb_{4.41}$). It is worthwhile to note that this is the first report on synthesizing electrocatalytic material including both alloy phases of PtSb and $PtSb_2$ in a catalyst system. Although some studies have reported that Pt-Sb combination affects to the selective glycerol oxidation reaction, understanding and revealing the specific catalytic role and function of active sites existed on PtSb and $PtSb_2$ alloy surfaces for the selective electrocatalytic oxidation of glycerol have not yet been established. This is important for providing future research guidance to design and develop novel electrocatalytic materials for selective production of DHA from biomass-derived glycerol. In order to understand how the reaction chemistry can be changed on the two alloy surfaces for the glycerol oxidation, we first characterized the synthesized Pt and Pt-Sb catalysts by a variety of physicochemical analyses to know the exact catalytic phase and state of the prepared samples. Then, we tested the prepared electrocatalysts in an electrochemical half cell and batch reactor system to confirm how the electrocatalytic performances could be changed according to the reaction conditions, such as the pH of the electrolyte, glycerol concentration, and electrode potential. First-principle density functional theory (DFT) calculations were also conducted to reveal and understand which catalytic site affects the active and selective reactions for DHA production from the EGOR and how the reaction chemistry in the EGOR changes with the Pt-Sb electrocatalysts compared to the Pt catalyst. These our efforts to understand the how and why of the selective production of the market-valued DHA chemical can be realized and at which specific active site of the prepared Pt-Sb electrocatalysts for the EGOR **(**Fig. 1**a)** are discussed and explored in the following section.

2. Experimental section

2.1. Electrocatalyst preparation

Pt-Sb (platinum and antimony) electrocatalysts were synthesized using a one-pot chemical synthesis method. In the method, chloroplatinic acid hexahydrate ($H_2PtCl_6{\cdot}6H_2O$) (ACS reagent, ≥ 37.50 % Pt basis, Sigma-Aldrich, St. Louis, MO, USA) and antimony (III) chloride ($SbCl_3$) (≥ 99.99 % trace metals basis, Sigma-Aldrich), and ethylene glycol (EG) (Reagent Plus®, ≥ 99 %, Sigma-Aldrich) were used as reagents. The synthesis procedure was as follows: In a 2-neck round flask (200 mL), $H_2PtCl_6{\cdot}6H_2O$ and $SbCl_3$ powders were mixed with 50 mL of EG. Note that the molarity of Pt was fixed at 50 mM in 50-mL EG, while the molarity of Sb was adjusted to set a Pt/Sb atomic ratio of 9:1, 7:3, 5:5, or 3:7. The mixture was stirred at 200 rpm overnight, followed by sonication for 1 h. The mixture was then heated at 200 °C for 4 h under N_2 purging with 200-rpm agitation. The heated mixture was cooled at room temperature for 1 h. Particles and supernatant liquid were separated from the resultant sample using a centrifuge, washed three times with acetone, and then dried at 200 °C overnight under vacuum. The dried powder was ground by hand, hydrogenation at 200 °C for 15 h under H_2 flow (30 mL min^{-1}), and then ground by hand again to obtain particle size of 100–170 nm. The resulting sample was used for glycerol oxidation reaction. Monometallic Pt electrocatalyst was also synthesized using same procedure with $H_2PtCl_6{\cdot}6H_2O$ and EG for comparison.

2.2. Electrocatalyst characterization

To characterize the crystal structure of electrocatalysts, X-ray diffraction (XRD) (SmartLab, Rigaku, Tokyo, Japan) patterns were recorded in the 2θ range of 10–90° at a scan speed of 2° min^{-1}. The actual metal contents of Pt and Sb in the synthesized electrocatalysts were measured by inductively coupled plasma optical emission spectroscopy (ICP-OES) (ICP-OES 720, Agilent Technologies, Santa Clara, CA, USA). The surface morphology and elemental composition were characterized using a field emission scanning electron microscopy (FE-SEM) (JSM-IT800, JEOL, Akishima, Tokyo, Japan) equipped with an energy-dispersive X-ray spectrometer (EDS) (XFlash 60, Bruker, Billerica, MA, USA). For lattice distance measurements of the electrocatalysts, a high-resolution transmission electron microscope (HR-TEM) (Tecnai G2 F30 S-TWIN, FEI, Hillsboro, OR USA) was used at an accelerating voltage of 300 kV. A double Cs-corrected TEM (Titan Cubed G2 60–300, FEI) was used to acquire high-angle annular dark-field scanning transmission electron microscopy (HAADF-STEM) images and

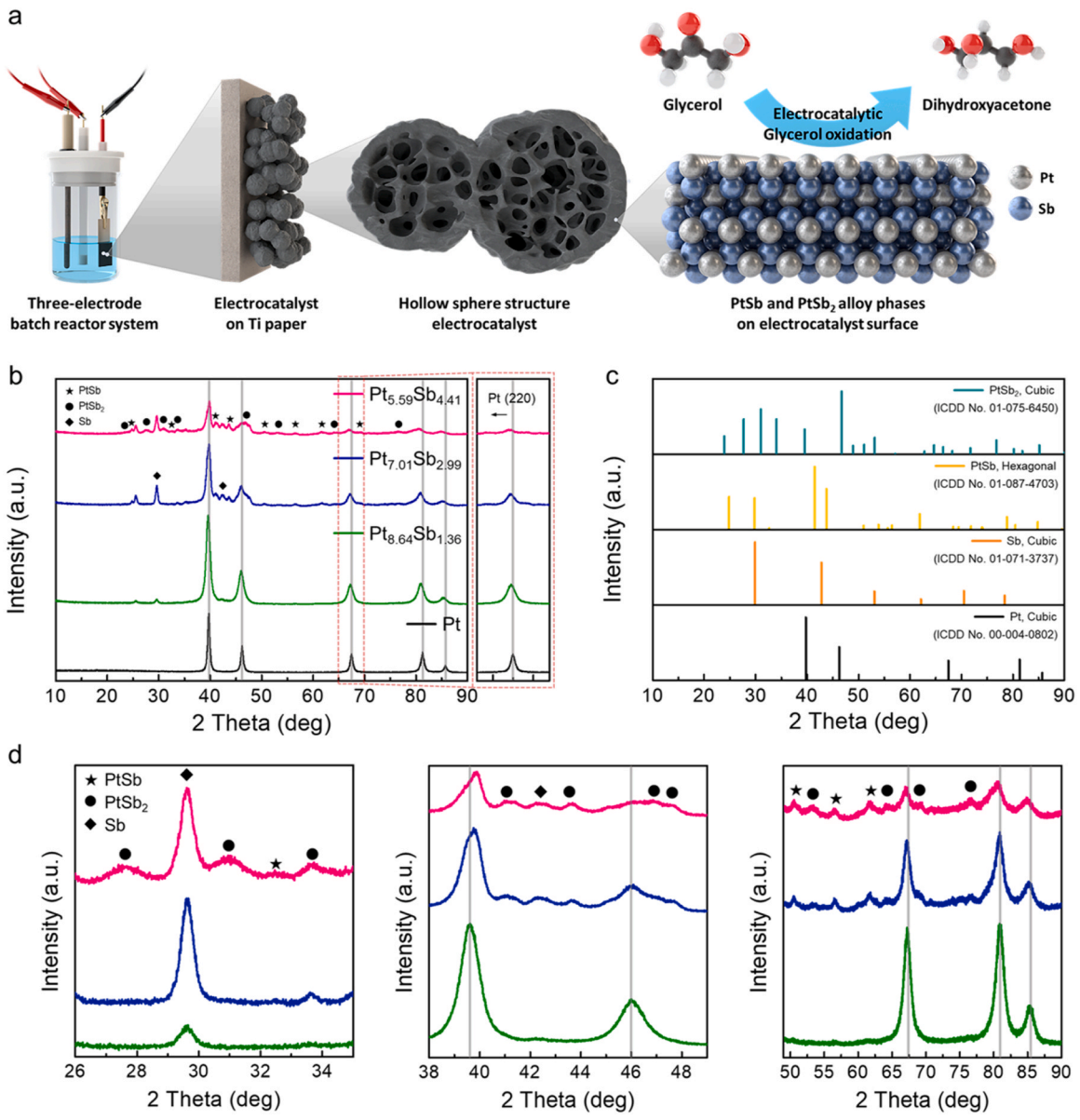

Fig. 1. Pt-Sb hollow sphere structure electrocatalysts synthesized via the simple one-pot chemical synthesis method for electrocatalytic glycerol oxidation reaction (EGOR). (a) Schematic illustration of the synthesized Pt-Sb hollow sphere electrocatalysts for selective production of DHA from the EGOR. (b) Xrd patterns of synthesized pt (black), $Pt_{8.64}Sb_{1.36}$ (Green), $Pt_{7.01}Sb_{2.99}$ (blue), and $Pt_{5.59}Sb_{4.41}$ (pink). (c) characteristic peaks of pt (Cubic, ICDD No. 00-004-0802), sb (Cubic, ICDD No. 01-071-3737), PtSb (Hexagonal, ICDD No. 01-087-4703) and $PtSb_2$ (Cubic, JCPDS No. 01-075-6450). (d) magnified XRD characteristic peak of $Pt_{8.64}Sb_{1.36}$ (Green), $Pt_{7.01}Sb_{2.99}$ (blue), and $Pt_{5.59}Sb_{4.41}$ (pink).

corresponding energy dispersive X-ray spectroscopy (EDS) elemental mapping. A multipurpose X-ray photoelectron spectroscopy (XPS, Sigma Probe, Thermo Fisher Scientific, Waltham, MA, USA) with an Al Kα source was performed to characterize the electronic structure of the electrocatalysts. In the X-ray photoelectron spectroscopy (XPS) data processing, all of the obtained XPS binding energy values were corrected on the basis of the C *1s* reference line at a value of 284.70 eV. Synchrotron-based X-ray absorption spectroscopy (XAS) at the K-edge of Pt, comprising X-ray absorption near the edge structure (XANES) and extended X-ray absorption fine structure (EXAFS) was performed at the 7D beamline of the Pohang Accelerator Laboratory (Pohang, Republic of Korea) using a Si (1 1 1) double crystal monochromator (PLS-II, 3.0 GeV).

2.3. Electrocatalytic performance measurement in an electrochemical half-cell system

Electrochemical half-cell tests were carried out at room temperature in a three-electrode system connected to a potentiostat (ZIVE MP2A, WonATech, Seoul, Korea) coupled with a rotating disk electrode (MSR Rotator, Pine Research Instrumentation, Durham, NC, USA). A catalyst-coated glassy carbon electrode (GCE) having 5-mm diameter and 0.196-cm^2 area was used as the working electrode. The working electrode was prepared by the following procedure. 10 mg of an electrocatalyst (Pt, $Pt_{8.64}Sb_{1.36}$, $Pt_{7.01}Sb_{2.99}$, or $Pt_{5.59}Sb_{4.41}$) was mixed with 1.00 mL of distilled water, 0.04 mL of 5 wt% Nafion® ionomer solution (D521, DuPont, Wilmington, DE, USA), and 0.20 mL of ethanol (95.0 %, Samchun Pure Chemical, Pyeongtaek, Korea). The mixture was then sonicated for 2 h, considered the electrocatalyst ink. After that, 0.01 mL of the fabricated catalyst ink was dropped on the GCE and then dried for

1 h. A graphite rod and Ag/AgCl (1 M KCl for acid and neutral) and Hg/HgO (1 M NaOH for base) were used counter and reference electrodes, respectively.

Polarization curve was obtained by the linear sweep voltammetry (LSV) method at a scan rate of 5 mV s^{-1} in the range of 0.054–1.254 V (*vs.* RHE) for acid, 0.449–1.649 V (*vs.* RHE) for neutral, and 0.007–1.307 V (*vs.* RHE) for base. The Tafel slope values were obtained from the *iR*-compensated LSV curve. The electrochemical impedance spectrum (EIS) were measured under a constant voltage of 0.454 V (*vs.* RHE) with acid, 0.850 V (*vs.* RHE) with neutral, and 0.508 V (*vs.* RHE) with base at frequencies between 100 kHz and 0.1 Hz with an AC amplitude of 5 mV. The electrochemical surface area (ECSA) was calculated by measuring the charges (Q_H) collected in the hydrogen adsorption-desorption peak area *via* cyclic voltammetry (CV) at a scan rate of 50 mV s^{-1} in 0.5 M H_2SO_4 using Eq. (1).

$$\mathrm{ECSA} = \mathrm{Q}_H \,/\, \mathrm{q}\ \mathrm{mg}_{\mathrm{Pt}} \tag{1}$$

The Q_H value represents the charge associated with hydrogen desorption, and the q value means the charge required to oxidize the hydrogen monolayer on Pt (210 μC cm^{-2}). The CV test was also carried out for 1000 cycles at the scan rate of 50 mV s^{-1} to test the stability of the electrocatalyst in glycerol oxidation. In addition to the ECSA measurements, LSV and CV electrochemical half-cell system tests were performed with 1 M glycerol in acid (0.5 M H_2SO_4, pH 0.3), neutral (0.1 M Na_2SO_4, pH 7), and base (0.1 M KOH, pH 13) under N_2 purging.

2.4. Electrocatalytic performance measurement in an electrochemical batch reactor system and product analysis

The same three-electrode cell system connected to a potentiostat was used to operate an electrochemical batch reactor system using an electrocatalyst-coated on titanium (Ti) paper (Bekaert, Zwevegem, Belgium) as a working electrode for electrocatalytic glycerol oxidation reaction (EGOR). The first step for fabricating the electrocatalyst-coated Ti papers was to prepare catalyst inks; through sonication for 1 h, 0.1 g of a prepared electrocatalyst was dispersed with 0.005 g of vulcan (XC-72) in a solution mixture of 0.40 mL of distilled water, 0.40 mL of 5 wt% Nafion® ionomer solution, and 2 mL of 2-propanol (99.5 %, Samchun Pure Chemical). This catalyst ink was spray-coated on Ti paper (geometric area: 2 cm), and dried in a convection oven at 100 °C for 0.5 h. The chronoamperometry (CA) method was performed to investigate the electrochemical properties in a 7 mL glycerol feed solution stirred at 400 rpm and maintained at 60 °C during EGOR. Before the CA test, the electrolyte was purged with N_2 gas for 30 min to remove the dissolved O_2 gas in the electrolyte.

After the EGOR testing, the reaction mixture solution was analyzed with the high-performance liquid chromatograph (HPLC) (YL9100, YL Instruments, Anyang, Korea) equipped with refractive index (RI) (RI-201 H, Shodex, Tokyo, Japan) and UV–vis (210 nm, YL9120, YL Instruments) detectors. An Aminex HPX-87H sugar column (Biorad, Hercules, CA, USA) was used at 60 °C. The mobile phase was 0.005 M H_2SO_4 (Samchun Pure Chemical) with a flow rate of 0.30 mL min^{-1}. After the reaction, liquid products were filtered with a 0.2-μm syringe filter. Then, a 1-μL liquid sample for each analysis was injected and analyzed with HPLC. The amount of glycerol consumed and the selectivities toward reaction products were quantified using external calibration curves of each. The chemicals used in the reactant solutions and standards were glycerol (GLY) (≥ 99.0 %, Product no. 27210S0350, Junsei Chemical, Tokyo, Japan), dihydroxyacetone (DHA) (Product no. PHR1430, Sigma-Aldrich), DL-lactic acid (LA) (≥85.0 % in water, Product no. L0226, Tokyo Chemical Industry, Tokyo, Japan), DL-glyceric acid (GLA) (20.0 % in water, Product no. D0602, Tokyo Chemical Industry), D-(+)-glyceraldehyde (GAD) (≥ 98.0 %, Product no. 49800, Sigma-Aldrich), glycolic acid (GCA) (≥ 98.0 %, Product no. G8284, Sigma-Aldrich), β-hydroxypyruvic acid (HPA) (≥ 95.0 %, Product no. 06372, Sigma-Aldrich), tartronic acid (TTA) (≥ 97.0 %, Product no. 86320, Sigma-Aldrich), and formic acid (FA) (85.0 %, Product no. F0182, Samchun Pure Chemical).

2.5. Computational details

We performed all the density functional theory (DFT) calculations in this work with the Vienna Ab initio Simulation Package (VASP) [60,61]. The generalized gradient approximation (GGA) with the Perdew-Burke-Ernzerhof (PBE) functional was adopted to describe the exchange-correlation energies and the projector augmented-wave (PAW) was employed to model the interactions between ions and electrons [62,63]. The non-covalent interactions was explained by the Grimme's DFT-D3 method [64]. The density of state (DOS) was calculated using VASP and VASPKit [65]. The d-band center value was also calculated using VASPKit. The kinetic energy cutoff was set to 520 eV, and. In all calculations, the Brillouin zone was sampled using a $3 \times 3 \times 1$ k-point grid. The k-points were generated using the Monkhorst-Pack method. The spin polarization was not considered. All structural optimizations were performed until the forces on all atoms became less than 0.03 eV/Å. We constructed three catalytic surfaces: PtSb(100), $PtSb_2$(111), and Pt(111). The number of Pt atoms was 96, 64 and 96 for the PtSb(100), $PtSb_2$(111) and Pt(111) surfaces, respectively. All surfaces were modeled with four layers, and only upper two layers and adsorbed molecules were allowed to relax during structural optimizations. A vacuum region was set to ~ 1.5 nm for all cases to avoid unphysical interactions between unit cells along the c-axis. The solvent effect in aqueous media was considered implicitly using the VASPsol [66,67].

Adsorption energy, E_{ad}, was calculated by

$$E_{ad} = E_{surface+adsorbate} + n_{H_2} * E_{H_2} - \left(E_{surface} + E_{GLY}\right) \tag{2}$$

where $E_{surface+adsorbate}$ was the total energy of the catalyst surface with the adsorbed molecule, and $E_{surface}$ was the energy of only catalyst surface without any adsorbate. The other energy terms, E_{H_2} and E_{GLY} were the energy of H_2 molecules and glycerol respectively. The number of generated H_2 molecules was denoted by n_{H_2}.

3. Results and discussion

3.1. Structural and chemical properties

All Pt and Pt-Sb-based hollow sphere structure electrocatalysts for the EGOR testing were synthesized *via* a simple one-pot chemical synthesis method using ethylene glycol as a reagent. The electrocatalysts were synthesized by varying the ratio of Pt to Sb (Pt_9Sb_1, Pt_7Sb_3, and Pt_5Sb_5), and the changes in the structure, physicochemical properties, electronic states, and electrochemical properties of the synthesized electrocatalysts were observed. After the synthesis of the Pt-Sb electrocatalysts, inductively coupled plasma optical emission spectroscopy (ICP-OES) analysis was performed to confirm that the Pt-Sb electrocatalysts in the intended ratios of Pt_9Sb_1, Pt_7Sb_3, and Pt_5Sb_5 were well synthesized. As can be seen in Table S1, the ICP-OES results demonstrated that the actual atomic ratios of the Pt_9Sb_1, Pt_7Sb_3, and Pt_5Sb_5 electrocatalysts were $Pt_{8.64}Sb_{1.36}$, $Pt_{7.01}Sb_{2.99}$, and $Pt_{5.59}Sb_{4.41}$, respectively.

We used X-ray diffraction (XRD) analysis to investigate the crystalline structure of the prepared Pt and Pt-Sb electrocatalysts as shown in Fig. 1**b–d**. Pt (Cubic, ICDD No. 00-004-0802), Sb (Cubic, ICDD No. 01-071-3737), PtSb (Hexagonal, ICDD No. 01-087-4703), and $PtSb_2$ (Cubic, ICDD No. 01-075-6450) phases were observed in synthesized electrocatalysts. In the XRD pattern of the synthesized Pt, the main characteristic diffraction peaks at approximately 39.75, 46.22, and 67.46 presented face-centered cubic (*fcc*) Pt peaks corresponding to (111), (200), and (220) planes, respectively. With the addition of about 10 % Sb into the Pt phase, the main diffraction peaks of the Sb(100) and

(110) phases were observed at 29.65 and 42.48 degrees. When the Sb content exceeded 30 %, the $Pt_{7.01}Sb_{2.99}$ and $Pt_{5.59}Sb_{4.41}$ catalysts detected PtSb(100), (002), (102), and (110) alloy phases at 24.80, 32.51, 41.15, and 43.64 degrees, respectively. The $PtSb_2$(211), (321), (024), and (511) alloy diffraction peaks at 33.67, 46.79, 52.97, 64.35, and 76.57 degrees were also observed along with the $PtSb_2$(311) major peak at 46.79 degrees. In particular, the $PtSb_2$(111), (200), and (210) characteristic peaks were additionally detected for the $Pt_{5.59}Sb_{4.41}$ catalyst compared to the $Pt_{7.01}Sb_{2.99}$ catalyst. As shown in Figs. 1**b and** 1**d**, the Pt(220) plane peak from the prepared Pt-Sb electrocatalysts appeared to have continuously shifted toward a lower angle compared to the Pt, indicating lattice expansion by formation of PtSb and $PtSb_2$ alloy phases [8,68,69]. The synthesized Pt-Sb electrocatalysts had a crystalline structure with a mixture of Pt, Sb, PtSb, and $PtSb_2$ phases. No metal oxides/hydroxides or other compounds were detected from the XRD measurements.

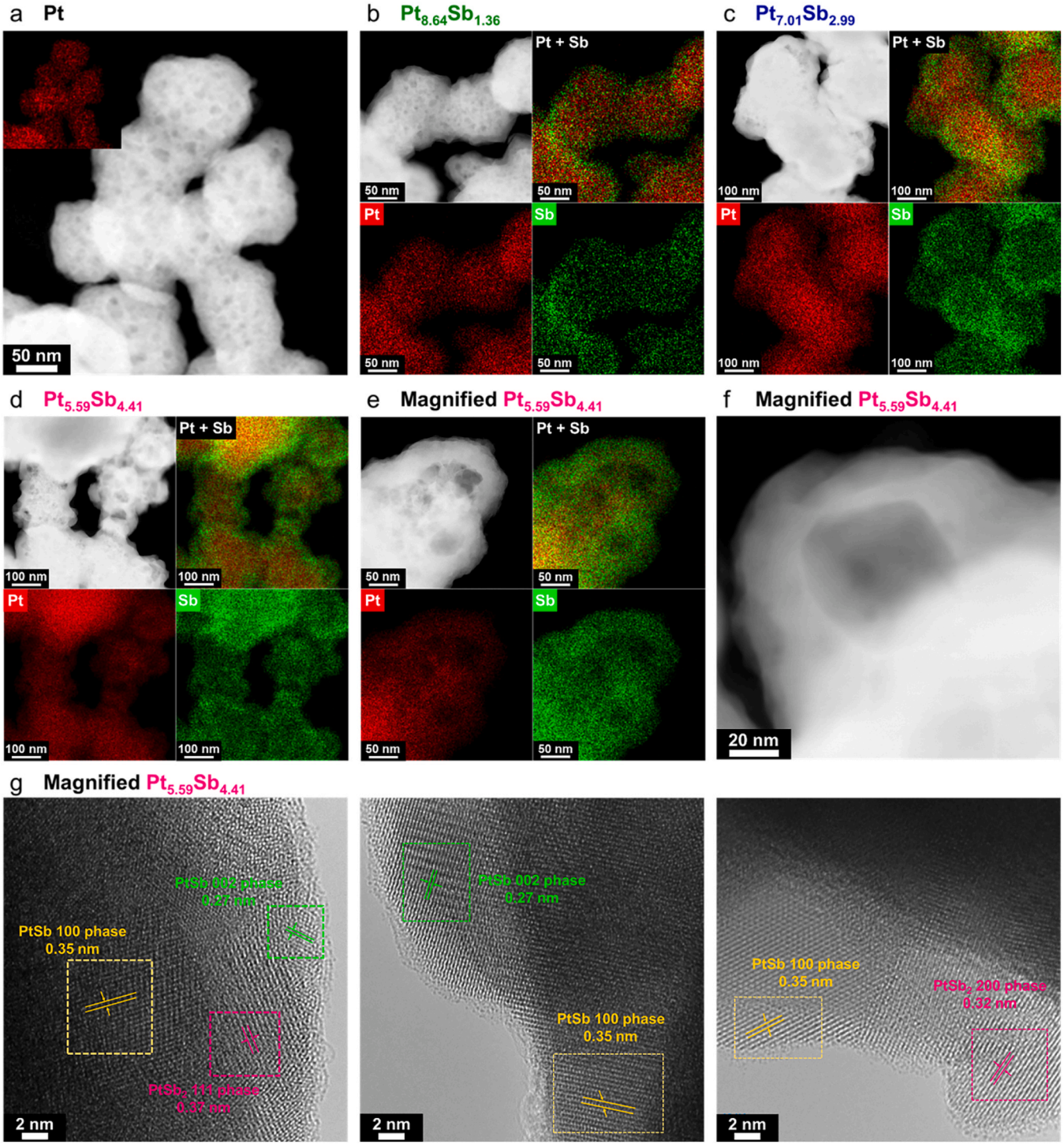

Fig. 2. Morphological analysis of the prepared electrocatalysts using electron microscopy. TEM images and corresponding EDS elemental mapping of Pt and Sb in a composite of Pt and Sb at synthesized (a) Pt, (b) $Pt_{8.64}Sb_{1.36}$, (c) $Pt_{7.01}Sb_{2.99}$, and (d) $Pt_{5.59}Sb_{4.41}$ electrocatalysts. (e) Enlarged HAADF-STEM image and EDS mapping images of $Pt_{5.59}Sb_{4.41}$ surface. (f) Additional enlarged HAADF-STEM image of $Pt_{5.59}Sb_{4.41}$ showing hollow spherical structure. (g) Lattice distance measurements for the Pt(111), PtSb(100 and 002), and $PtSb_2$(111) phases measured in the HR-TEM image of $Pt_{5.59}Sb_{4.41}$ surface.

The surface morphology and elemental composition of the prepared Pt-Sb electrocatalysts were analyzed by field emission scanning electron microscopy (FE-SEM) equipped with an energy-dispersive X-ray spectrometer (EDS), as shown in Fig. S1–S2 **and** Table S2. The Pt and Pt-Sb electrocatalysts appeared to be formed as spherical particles, and the particle size increased as the content of Sb increased. This was likely due to the result of lattice expansion by the incorporation of Sb into a Pt lattice, as shown in Figs. 1**b and** 1**d** of the XRD characterization. The

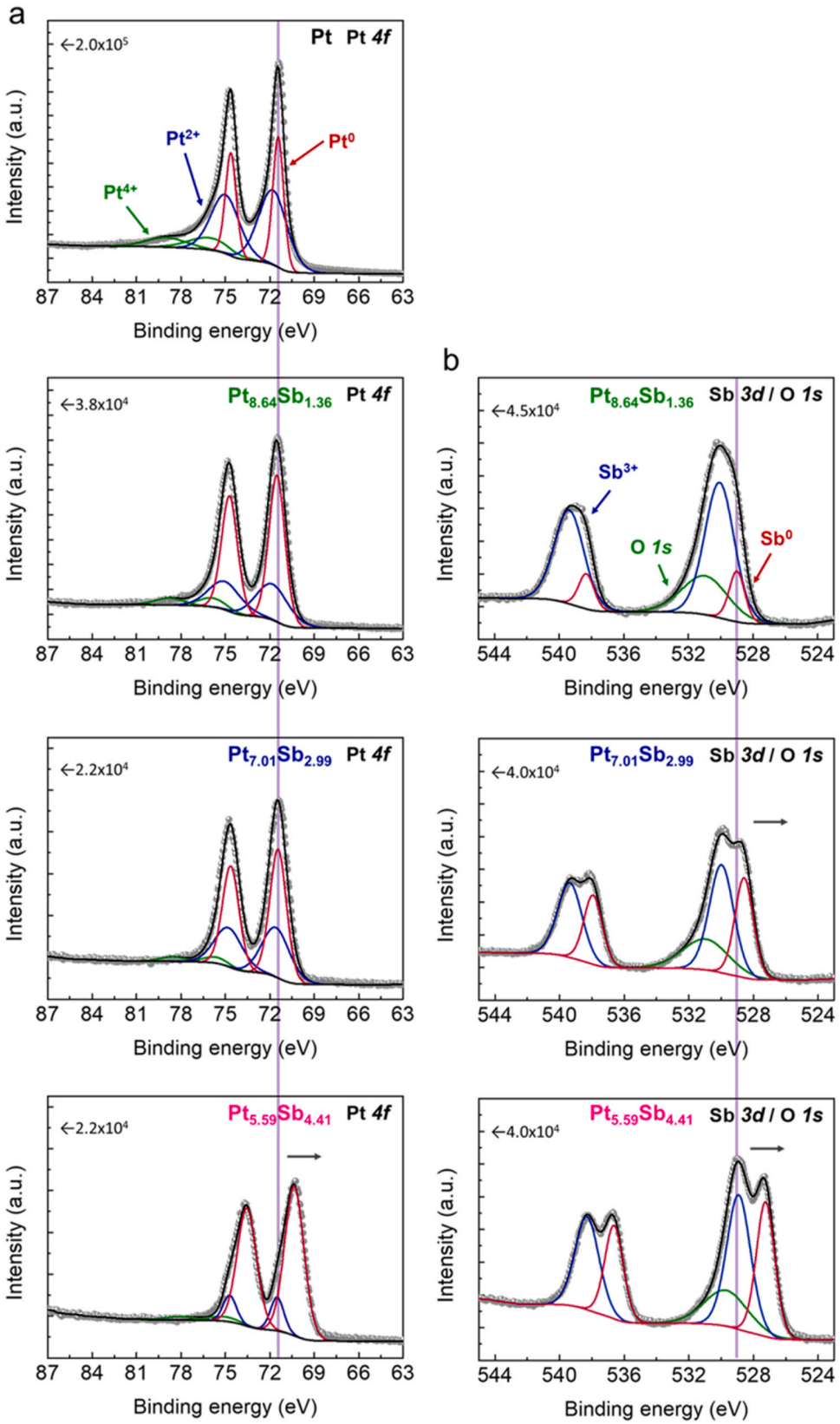

Fig. 3. Chemical and electronic analysis of the XPS spectra of (a) Pt *4f* and (b) Sb *3d*/O *1s* for the synthesized Pt, $Pt_{8.64}Sb_{1.36}$, $Pt_{7.01}Sb_{2.99}$, and $Pt_{5.59}Sb_{4.41}$.

particle size distributions of Pt and Pt-Sb electrocatalysts were approximately 102 ± 14 nm to 172 ± 29 nm in size, which were obtained by measuring the size of about 100 particles based on the SEM image as shown in Fig. S3. The bulk ratio of Pt and Sb in the synthesized electrocatalysts showed results similar to ICP-OES, as shown in the elemental mapping results in Table S2.

We carried out transmission electron microscopy (TEM) analysis coupled with corresponding EDS to measure the detailed crystallographic structure and elemental distribution of the synthesized Pt, $Pt_{8.64}Sb_{1.36}$, $Pt_{7.01}Sb_{2.99}$, and $Pt_{5.59}Sb_{4.41}$ electrocatalysts. The EDS mapping data corresponds to the respective high-angle annular dark-field scanning TEM (HAADF-STEM) images, as shown in Fig. 2 **and** Fig. S4–S7. The HAADF-STEM and corresponding EDS mapping images of synthesized Pt in Fig. 2**a and** Fig. S4 confirm that the hollow sphere structure was synthesized, and the Pt element was uniformly distributed. As shown in the TEM images of the Pt-Sb electrocatalysts synthesized at various Pt to Sb ratios in Fig. 2**b–g and** Fig. S5–S7, the hollow sphere structure was well maintained in spite of the addition of Sb. EDS line scan data was also obtained by scanning the enlarged image in the direction of the yellow arrow in Fig. S5–S7. It was confirmed that the distribution of the Sb element on the surface of the synthesized Pt-Sb hollow structure catalysts increased with the increase of Sb content in the order of $Pt_{8.64}Sb_{1.36}$, $Pt_{7.01}Sb_{2.99}$, and $Pt_{5.59}Sb_{4.41}$ electrocatalysts. Fig. 2**f** demonstrated that the Pt-Sb hollow spherical structure was confirmed through the enlarged HAADF-STEM image. The high-resolution TEM images **(**Fig. 2**g)** of the synthesized $Pt_{5.59}Sb_{4.41}$ hollow sphere structure exhibited atomic lattice distances of 0.23 nm, 0.35 nm, 0.27 nm, and 0.37 nm, which corresponded to the Pt(111), PtSb(100 and 002), and $PtSb_2$(111) phases, respectively [70,71]. The lattice distances were also confirmed by referring to the d-spacing values of the powder diffraction reference ICDD number. This indicates that the synthesized $Pt_{5.59}Sb_{4.41}$ electrocatalyst has mixed crystal phase structures of Pt, PtSb, and $PtSb_2$, which is consistent with the XRD results.

3.2. Electronic properties

The surface chemical states and electronic structures of the prepared Pt, $Pt_{8.64}Sb_{1.36}$, $Pt_{7.01}Sb_{2.99}$, and $Pt_{5.59}Sb_{4.41}$ electrocatalysts were investigated by X-ray photoelectron spectroscopy (XPS), as shown in Fig. 3**,** Fig. S8**,** Table 1**, and** Table S3. We present the XPS spectra in the Pt *4f*, Sb *3d*, O *1s*, and C *1s* regions for the Pt, $Pt_{8.64}Sb_{1.36}$, $Pt_{7.01}Sb_{2.99}$, and $Pt_{5.59}Sb_{4.41}$ electrocatalysts and tabulate the respective peak assignment and binding energy of deconvoluted peaks from the XPS spectra. XPS binding energies were corrected by referencing the C *1s* line at 284.70 eV in Fig. S8. As presented in the Pt *4f* spectra of the prepared electrocatalysts in Fig. 3**a**, the individual Pt $4f_{7/2}$ and Pt $4f_{5/2}$ doublets were deconvoluted into three oxidation states of metallic Pt^0 (Pt: 71.43 eV and 74.63 eV, $Pt_{8.64}Sb_{1.36}$: 71.52 eV and 74.72 eV, $Pt_{7.01}Sb_{2.99}$: 71.44 eV and 74.64 eV, and $Pt_{5.59}Sb_{4.41}$: 70.35 eV and 73.55 eV), oxide Pt^{2+} (Pt: 71.80 eV and 75.00 eV, $Pt_{8.64}Sb_{1.36}$: 71.82 eV and 75.02 eV, $Pt_{7.01}Sb_{2.99}$: 71.59 eV and 74.79 eV, and $Pt_{5.59}Sb_{4.41}$: 71.51 eV and 74.71 eV), and oxide Pt^{4+} (Pt: 76.10 eV and 79.00 eV, $Pt_{8.64}Sb_{1.36}$: 75.88 eV and 78.78 eV, $Pt_{7.01}Sb_{2.99}$: 75.67 eV and 78.57 eV, and $Pt_{5.59}Sb_{4.41}$: 75.16 eV and 78.06 eV). Metallic Pt^0 was dominant in all the prepared electrocatalysts. The measured Pt $4f_{7/2}$ metallic peak appears at a higher binding energy than the commonly reported value for metallic Pt^0 (~ 71.4 eV), which is a characteristic feature of the hollow nanostructure. As the particle size increases, this peak shifts toward lower binding energies, indicating a size-dependent electronic effect, as shown in Fig. 3 **and** Table 1 [72–75]. The Full Width at Half Maximum (FWHM) values of the Pt *4f* peak were adjusted based on the Pt to Sb atomic ratio in each electrocatalyst. These changes reflect variations in the electronic state of Pt across different Pt-Sb compositions ($Pt_{8.64}Sb_{1.36}$, $Pt_{7.01}Sb_{2.99}$, and $Pt_{5.59}Sb_{4.41}$), which can influence the FWHM in the XPS spectra. As the Sb content increases, the crystallinity and particle size of the electrocatalysts also increase, contributing to the observed decrease in the FWHM [74–76]. The shift in Pt *4f* binding energy with increasing Sb content is attributed to changes in the electronic structure associated with alloy formation, particularly the emergence of PtSb and $PtSb_2$ phases. As the Sb content increases, the Pt^0 peak initially shifts to higher binding energy, possibly due to surface effects or partial oxidation, and then shifts to lower values as alloying progresses and the oxidation state decreases. This reflects variations in the interaction strength between Pt and Sb. This trend is also observed in the white line intensity of the XANES spectra, indicating a gradual transition from oxidized Pt species to metallic Pt-Sb bonding environments. At the $Pt_{7.01}Sb_{2.99}$ composition, strong Pt-Sb interactions begin to form, leading to the development of a PtSb alloy phase. With further Sb addition, the $PtSb_2$ phase becomes predominant. The broadening of the Pt^0 peak suggests a mixed oxidation state or coordination environment, likely due to the coexistence of multiple phases and interfacial structures. This interpretation aligns with the general understanding that homogeneous crystalline phases yield sharper XPS peaks, whereas structurally diverse environments result in broader peak shapes. For the Sb *3d* XPS spectra in Fig. 3**b**, the Sb $3d_{5/2}$ and Sb $3d_{3/2}$ doublets were also deconvoluted into two distinguishable peaks. These peaks corresponded to metallic Sb^0 ($Pt_{8.64}Sb_{1.36}$: 529.00 eV and 538.31 eV, $Pt_{7.01}Sb_{2.99}$: 528.58 eV and 537.93 eV, and $Pt_{5.59}Sb_{4.41}$: 527.26 eV and 536.63 eV) and oxide Sb^{3+} ($Pt_{8.64}Sb_{1.36}$: 530.08 eV and 539.38 eV, $Pt_{7.01}Sb_{2.99}$: 529.98 eV and 539.36 eV, and $Pt_{5.59}Sb_{4.41}$: 528.92 eV and 538.30 eV). As the amount of added Sb increased, the peak intensity of metallic Sb^0 also increased. The Sb *3d* spectrum contained an overlapping peak, which was the O *1s* ($Pt_{8.64}Sb_{1.36}$: 530.96 eV, $Pt_{7.01}Sb_{2.99}$: 530.96 eV, and $Pt_{5.59}Sb_{4.41}$: 529.70 eV) oxygen peak. Interestingly, it was observed that the binding energy of metallic Pt^0 and Sb^0 phases in the prepared $Pt_{5.59}Sb_{4.41}$ electrocatalyst shifted negatively to higher values (Pt: 1.45 eV and Sb: 1.74 eV). This phenomenon can be associated with electronic interactions between Pt and Sb atomic orbitals by the formation of Pt-Sb alloys such as PtSb and $PtSb_2$. An increase in the electron density around Pt can also lead to partial filling of the Pt *5d* band, resulting in a downshift of the *d* band center. The Pt *d*-band center shift affected the adsorption strength with reaction molecules such as O_2 and H_2, suggesting that it can improve the catalytic activity and durability for electrocatalytic reactions [77–83].

Table 1
XPS peak assignment and binding energy values of deconvoluted peaks for the synthesized Pt, $Pt_{8.64}Sb_{1.36}$, $Pt_{7.01}Sb_{2.99}$, and $Pt_{5.59}Sb_{4.41}$.

	XPS peak assignment					
Catalyst	**Pt *4f* (eV)**					
	Pt^0 $4f_{7/2}$	Pt^0 $4f_{5/2}$	Pt^{2+} $4f_{7/2}$	Pt^{2+} $4f_{5/2}$	Pt^{4+} $4f_{7/2}$	Pt^{4+} $4f_{5/2}$
Pt	71.43	74.63	71.80	75.00	76.10	79.00
$Pt_{8.64}Sb_{1.36}$	71.52	74.72	71.82	75.02	75.88	78.78
$Pt_{7.01}Sb_{2.99}$	71.44	74.64	71.59	74.79	75.67	78.57
$Pt_{5.59}Sb_{4.41}$	70.35	73.55	71.51	74.71	75.16	78.06
Catalyst	**Sb *3d* (eV)**					**O *1s* (eV)**
	Sb^0 $3d_{5/2}$	Sb^0 $3d_{3/2}$	Sb^{3+} $3d_{5/2}$	Sb^{3+} $3d_{3/2}$	Sb^0 $3d_{5/2}$	-
Pt	-	-	-	-	-	-
$Pt_{8.64}Sb_{1.36}$	529.00	538.31	530.08	539.38	530.96	529.00
$Pt_{7.01}Sb_{2.99}$	528.58	537.93	529.98	539.36	530.96	528.58
$Pt_{5.59}Sb_{4.41}$	527.26	536.63	528.92	538.30	529.70	527.26

3.3. Synchrotron-based analysis on the local atomic structure

All the prepared samples were further studied by X-ray absorption spectroscopy (XAS) in order to determine the electronic and local structure around Pt atoms in Fig. 4 **and** Table 2. The X-ray absorption near the edge structure (XANES) spectra of Pt-Sb catalyst samples measured at the Pt L_3 edge **(**Fig. 4**a)** exhibits spectral features similar to

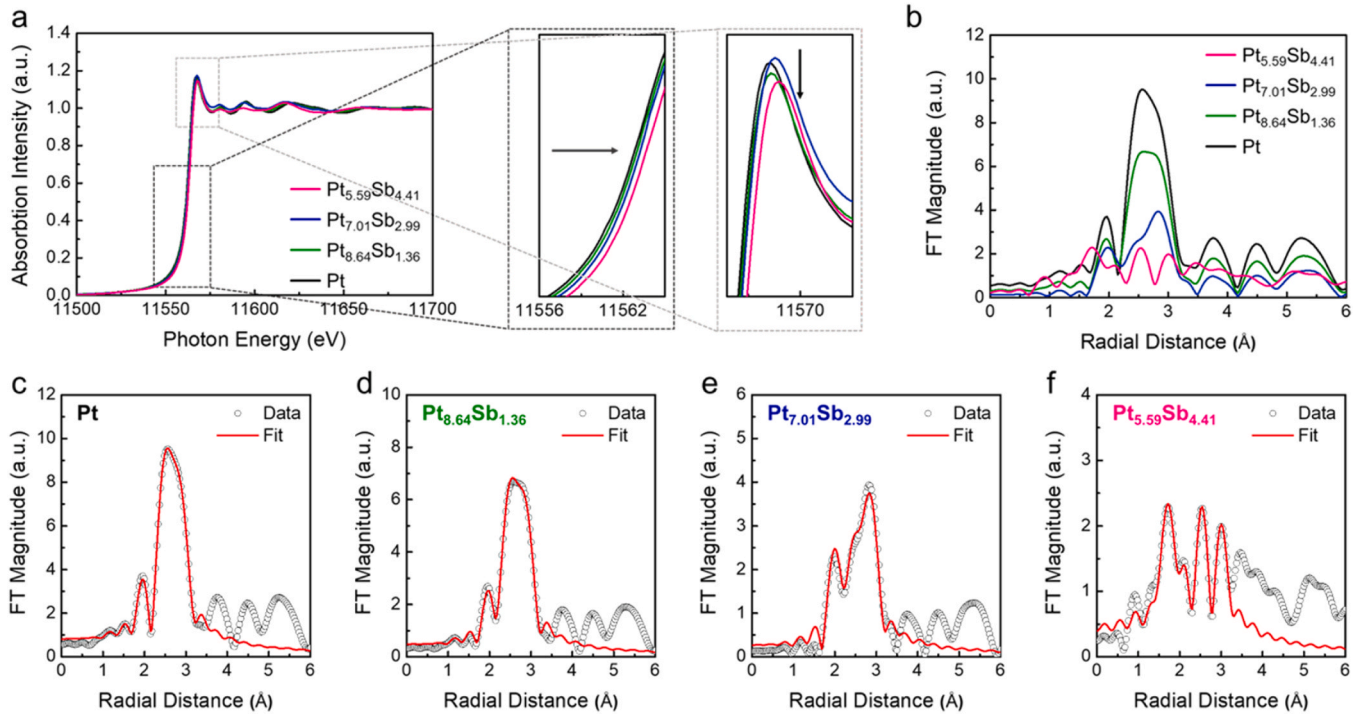

Fig. 4. Synchrotron-based XAS analysis of the prepared electrocatalysts with normalized (a) XANES and (b) EXAFS spectra at Pt *k*-edge. Pt l_3-edge EXAFS fitting data for (c) pt, (d) $Pt_{8.64}Sb_{1.36}$, (e) $Pt_{7.01}Sb_{2.99}$, and (f) $Pt_{5.59}Sb_{4.41}$.

Table 2
Summary of Pt l_3-edge EXAFS fitting results of the prepared Pt, $Pt_{8.64}Sb_{1.36}$, $Pt_{7.01}Sb_{2.99}$, and $Pt_{5.59}Sb_{4.41}$ electrocatalysts.

Catalyst	Edge	Shell	N^a	R^b (Å)	R factor[c] (%)
Pt	Pt L_3	Pt-Pt	8.60 ± 0.47	2.763 ± 0.002	0.0009
$Pt_{8.64}Sb_{1.36}$	Pt L_3	Pt-Pt	5.85 ± 0.64	2.773 ± 0.007	0.0029
		$Pt\text{-}Sb_{(PtSb)}$	0.25 ± 0.20	2.754 ± 0.051	
$Pt_{7.01}Sb_{2.99}$	Pt L_3	Pt-Pt	4.45 ± 0.91	2.758 ± 0.009	0.0136
		$Pt\text{-}Sb_{(PtSb)}$	0.80 ± 0.21	2.668 ± 0.017	
$Pt_{5.59}Sb_{4.41}$	Pt L_3	Pt-Pt	2.33 ± 0.67	2.831 ± 0.013	0.0053
		$Pt\text{-}Sb_{(PtSb)}$	1.54 ± 0.43	2.706 ± 0.434	
		$Pt\text{-}Sb_{(PtSb2)}$	0.70 ± 0.56	2.363 ± 0.033	

[a] Coordination number.
[b] Distance between absorber and backscatter atoms.
[c] A goodness of curve fitting; $S_0^2 = 0.9$ for Pt; Fitting range: $1.4 < R$ (Å) < 3.3 Å.

those of pure Pt, indicating that Pt in Pt-Sb system predominantly exists in the metallic state (Pt^0). A detailed analysis of the edge region reveals that the edge energy shifts toward higher energies as the Sb content increases, suggesting an enhancement of intermetallic interactions between Pt and Sb [84]. Notably, a decrease in white line intensity is observed in the case of $Pt_{5.59}Sb_{4.41}$, which is consistent with the increased Pt 5*d* electron density detected by XPS analysis. This finding implies that Sb addition modifies the electronic structure of Pt. Fig. 4**b–f** presents the k^3-weighted Fourier-transformed extended X-ray absorption fine structure (EXAFS) data. Table 2 provides the corresponding fitting results. The relative intensity of the characteristic Pt-Pt scattering peak decreases as the Sb content increases, while distinct Pt-Sb scattering peaks emerge. Specifically, the Pt-Pt coordination number decreases from 5.85 to 2.33, whereas the Pt-Sb coordination number associated with PtSb alloy formation increases from 0.25 to 1.54. In particular, the $Pt_{5.59}Sb_{4.41}$ sample exhibits newly formed Pt-Sb interactions attributed to the $PtSb_2$ phase, further corroborating the presence of $PtSb_2$ as identified in XRD and TEM analyses. An investigation of the Pt-Pt and Pt-Sb bond lengths as a function of Sb addition reveals a nonlinear variation in the Pt-Pt bond distance. In pure Pt, the Pt-Pt bond length is measured at 2.763 Å, whereas it slightly increases to 2.773 Å in $Pt_{8.64}Sb_{1.36}$ but decreases to 2.758 Å in $Pt_{7.01}Sb_{2.99}$. The Pt-Pt bond length further increases to 2.831 Å in $Pt_{5.59}Sb_{4.41}$, reflecting lattice expansion due to Sb incorporation. As the Pt-Pt bond length increases, the interaction between Pt atoms weakens, potentially leading to a downshift of the *d*-band center. In particular, the $Pt_{5.59}Sb_{4.41}$ sample with the longest Pt-Pt bond length is expected to have the lowest *d*-band center, influencing the adsorption energy of reaction intermediates on the catalyst surface. Meanwhile, the Pt-Sb bond length progressively decreases with increasing Sb content. In $Pt_{8.64}Sb_{1.36}$, the Pt-Sb bond length is measured at 2.754 Å, while it shortens to 2.668 Å in $Pt_{7.01}Sb_{2.99}$. In $Pt_{5.59}Sb_{4.41}$, two distinct Pt-Sb bond lengths of 2.706 Å and 2.363 Å are observed. The Pt-Sb bond length of 2.363 Å indicates strong Pt-Sb interactions characteristic of the $PtSb_2$ phase. These results suggest the coexistence of both PtSb and $PtSb_2$ phases in the $Pt_{5.59}Sb_{4.41}$ sample, leading to the formation of multiple interfaces within the catalyst. The multi-interface structure is expected to modulate the electronic structure of active sites, enhance reaction kinetics, and ultimately contribute to improved catalytic performance.

Additionally, Pt and Sb were synthesized in an intended ratio of Pt_3Sb_7 to determine how the structural and electronic properties of the Pt_3Sb_7 catalyst can be changed compared to the prepared Pt-Sb electrocatalysts. The XRD analysis of the synthesized Pt_3Sb_7 sample confirmed the presence of PtSb and $PtSb_2$ alloy phases seen in the electrocatalysts with $Pt_{5.59}Sb_{4.41}$ in Fig. S9. As shown in the ICP-OES and EDS elemental data in Fig. S10b **and** Table S4, it was synthesized in the actual composition of $Pt_{6.06}Sb_{3.94}$ despite the high amount of added Sb (Pt:Sb = 3:7), which has a composition similar to the $Pt_{5.59}Sb_{4.41}$ sample.

The SEM and TEM analyses demonstrated that particles similar in size to $Pt_{5.59}Sb_{4.41}$ were synthesized, and the Sb content was mainly distributed on the particle surface of Pt-Sb in Fig. S10a–S11. In Fig. S12 **and** Table S5, the synthesized $Pt_{6.06}Sb_{3.94}$ electrocatalysts show that the metallic Pt^0 and Sb^0 phases are dominant, but the metallic Sb^0 phase has a lower intensity and little binding energy shift compared to $Pt_{5.59}Sb_{4.41}$. As a result, the electrocatalyst ($Pt_{6.06}Sb_{3.94}$) with a composition similar to the $Pt_{5.59}Sb_{4.41}$ sample was synthesized, even with increasing the Sb content. This indicates that there was no additional effect of composition change with an increasing Sb content.

3.4. Electrocatalytic properties

We conducted electrocatalytic performance testing in an electrochemical half-cell system using the synthesized Pt, $Pt_{8.64}Sb_{1.36}$, $Pt_{7.01}Sb_{2.99}$, and $Pt_{5.59}Sb_{4.41}$ electrocatalysts to investigate the catalytic effect of the electrocatalysts with different phases, namely, PtSb and $PtSb_2$ alloys for the EGOR. The prepared Pt-Sb electrocatalysts were deposited on the glassy carbon electrode (GCE) as a working electrode with an active geometric area of 0.196 cm. We measured the electrochemical performances for the EGOR using linear sweep voltammetry (LSV) and cyclic voltammetry (CV) methods in an N_2-purged 1 M glycerol under different electrolyte solutions (acid: 0.5 M H_2SO_4, pH 0.3, neutral: 0.1 M Na_2SO_4, pH 7, and base: 0.1 M KOH, pH 13) at room temperature. Fig. 5 shows the change of the EGOR properties on the prepared Pt-Sb electrocatalysts. The electrocatalytic activity parameters of the prepared catalysts are summarized in Table 3 **and** Table S6. Fig. 5**a–c** exhibit the LSV curves related to the current density (current divided by geometric area, mA cm^{-2}) of the Pt-Sb electrocatalysts at different pH conditions. To understand how the electrochemical reaction kinetics changes with the prepared electrocatalysts, we calculated the Tafel slopes and onset potential for the EGOR over prepared electrocatalysts based on the current density of the LSV curve in Fig. 5**a–c**. The Tafel slope values were obtained from *iR*-compensation LSV curves. As shown in Table S6, among the tested Pt and Pt-Sb electrocatalysts, the Tafel slope of the $Pt_{5.59}Sb_{4.41}$ electrocatalyst showed lower values in acid (Pt: 239 ± 4 eV $dec^{-1}$and $Pt_{5.59}Sb_{4.41}$: 179 ± 5 eV dec^{-1}) and neutral (Pt: 234 ± 9 eV $dec^{-1}$and $Pt_{5.59}Sb_{4.41}$: 197 ± 2 eV dec^{-1}), but slightly higher values in base (Pt: 160 ± 1 eV $dec^{-1}$and $Pt_{5.59}Sb_{4.41}$: 180 ± 1 eV dec^{-1}). In addition, the $Pt_{5.59}Sb_{4.41}$ electrocatalyst significantly demonstrated lower onset potential values in acid [0.332 ± 0.006 V (V *vs.* RHE)] and base [0.329 ± 0.001 V (V *vs.* RHE)] but similar values to other electrocatalysts in neutral [0.699 ± 0.006 V (V *vs.* RHE)]. These results confirmed that the onset potential values were dramatically lower in the base conditions in Fig. 5**c and** Table 3. The results indicate that the $Pt_{5.59}Sb_{4.41}$ electrocatalyst composed of mixed phase with PtSb

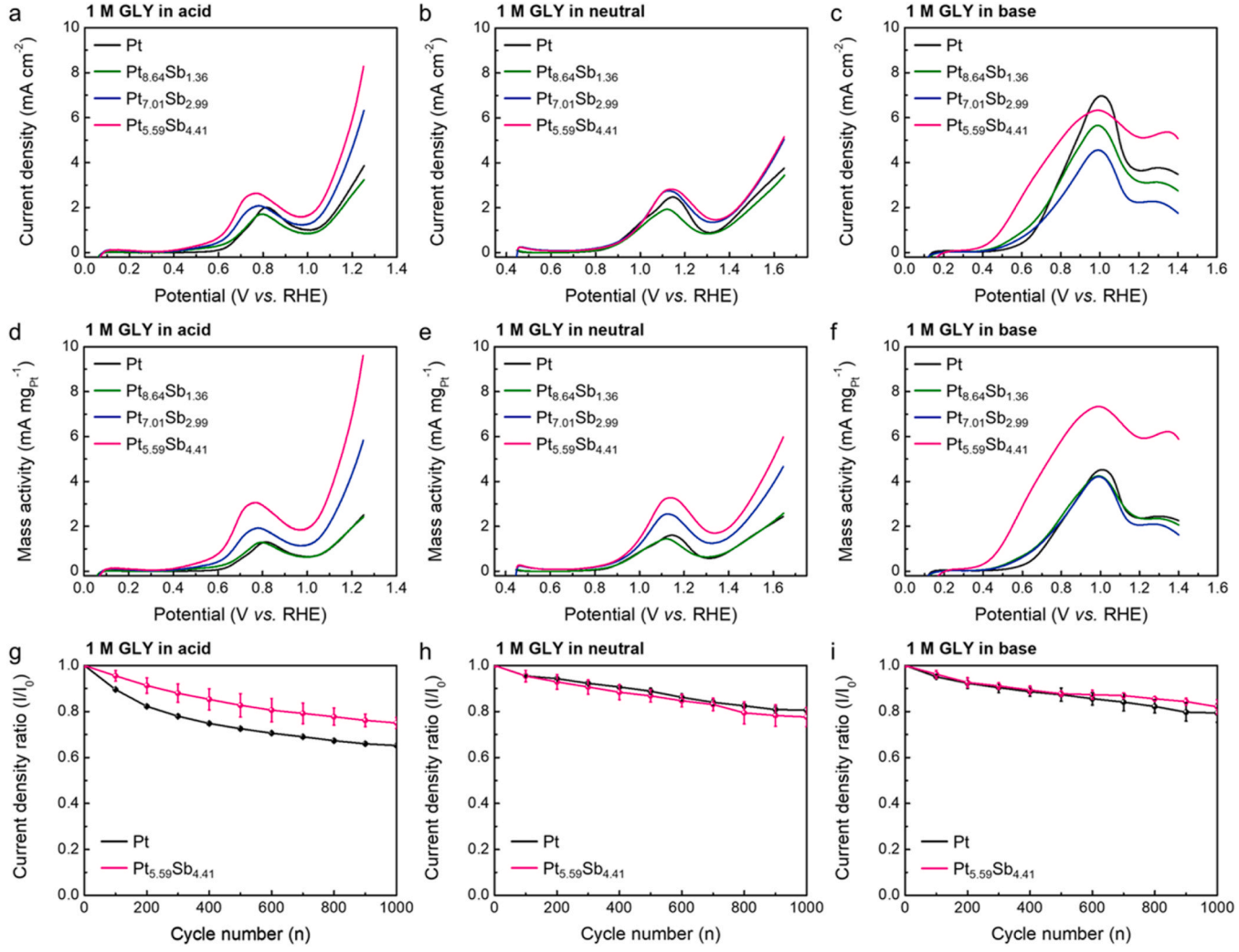

Fig. 5. Electrochemical performance analysis of prepared Pt, $Pt_{8.64}Sb_{1.36}$, $Pt_{7.01}Sb_{2.99}$, and $Pt_{5.59}Sb_{4.41}$ electrocatalysts for the EGOR in electrochemical half-cell system using the rotating disk electrode. Lsv curves and cycle stability results of prepared electrocatalysts loaded onto a glassy carbon electrode in 1 M glycerol with 0.5 M H_2SO_4 (acid, pH 0.3), 0.1 M Na_2SO_4 (neutral, pH 7), and 0.1 M KOH (base, pH 13) electrolytes. (a–c) Show current density (current divided by electrode geometric area, mA cm^{-2}). (d-f) represent mass activity (current divided by Pt mass, mA mg_{Pt}^{-1}). (g-I) indicate the cycle stability plot.

Table 3
Electrocatalytic activity comparison of the prepared Pt, $Pt_{8.64}Sb_{1.36}$, $Pt_{7.01}Sb_{2.99}$, and $Pt_{5.59}Sb_{4.41}$ electrocatalysts for the EGOR. Onset potential and mass activity (current divided by Pt mass, mA mg_{Pt}^{-1}) were obtained from the LSV curves in Fig. 5.

Catalyst	Onset potential (V *vs.* RHE) in acid	Onset potential (V *vs.* RHE) in neutral	Onset potential (V *vs.* RHE) in base	Mass activity (mA mg_{Pt}^{-1}) at 0.65 (V *vs.* RHE) in acid	Mass activity (mA mg_{Pt}^{-1}) at 0.96 (V *vs.* RHE) in neutral	Mass activity (mA mg_{Pt}^{-1}) at 0.60 (V *vs.* RHE) in base
Pt	0.446 ± 0.015	0.664 ± 0.013	0.419 ± 0.004	0.230 ± 0.008	0.624 ± 0.004	0.272 ± 0.015
$Pt_{8.64}Sb_{1.36}$	0.359 ± 0.008	0.674 ± 0.014	0.356 ± 0.004	0.373 ± 0.004	0.579 ± 0.003	0.675 ± 0.004
$Pt_{7.01}Sb_{2.99}$	0.350 ± 0.005	0.680 ± 0.007	0.347 ± 0.006	0.782 ± 0.006	0.800 ± 0.023	0.615 ± 0.007
$Pt_{5.59}Sb_{4.41}$	0.332 ± 0.006	0.699 ± 0.006	0.329 ± 0.001	1.460 ± 0.033	0.967 ± 0.016	2.866 ± 0.008

and $PtSb_2$ alloys may affect the excellent electrocatalytic kinetics for the EGOR. The electrocatalytic reaction activity of the EGOR is enhanced due to the formation of PtSb and $PtSb_2$ alloys. This can be also supported by the fact that the current density values of $Pt_{5.59}Sb_{4.41}$ for the EGOR tend to increase overall compared to other prepared electrocatalysts regardless of pH condition.

Fig. 5**d-f,** Table 3**, and** Table S6 present mass activity (current divided by Pt mass, mA mg_{Pt}^{-1}) and specific activity (current divided by electrochemical surface area (ECSA), mA cm_{ECSA}^{-2}) values calculated based on generated current at different pH conditions for the EGOR. To calculate the ECSA values, the CV method in the 0.5 M H_2SO_4 electrolyte at room temperature was used to examine the H_2 adsorption/desorption behavior of the Pt, $Pt_{8.64}Sb_{1.36}$, $Pt_{7.01}Sb_{2.99}$, and $Pt_{5.59}Sb_{4.41}$ electrocatalysts as shown in Fig. S13 **and** Table S6. The ECSA values measured for Pt, $Pt_{8.64}Sb_{1.36}$, $Pt_{7.01}Sb_{2.99}$, and $Pt_{5.59}Sb_{4.41}$ were 16.524, 11.819, 29.314, and 27.219 cm, respectively. The $Pt_{5.59}Sb_{4.41}$ electrocatalyst represents higher mass activity values than other prepared electrocatalysts at all the acid, neutral and base conditions. However, the specific activity values of the $Pt_{5.59}Sb_{4.41}$ electrocatalyst were slightly higher but similar values compared to those of other tested electrocatalysts as presented in Table S6. The ECSA values of $Pt_{5.59}Sb_{4.41}$ and $Pt_{7.01}Sb_{2.99}$ electrocatalysts tended to be larger than those of the other two synthesized catalysts despite the larger particle size due to the formation of Pt-Sb alloys as shown in the SEM images of Fig. S1. It should be noted that Sb only is not involved in the electrochemical EGOR performance and the ECSA value increases as the amount of Pt decreases. This shows that the glycerol oxidation reactivity increases as the PtSb and $PtSb_2$ alloys are formed. The enhanced ECSA values also indicate that introducing Sb to Pt optimized the Pt-Sb electrocatalysts with more electrochemically active sites[85–87]. As presented in Fig. S14, the CV data also revealed that the $Pt_{5.59}Sb_{4.41}$ electrocatalyst with formation of PtSb and $PtSb_2$ alloys had higher Pt mass activity than other tested electrocatalysts in all the acid, neutral, and base conditions. In the results of electrochemical impedance spectroscopy (EIS) analysis in Fig. S15, the Nyquist plot of the $Pt_{5.59}Sb_{4.41}$ electrocatalyst shows that the semicircle size is smaller than that of other electrocatalysts in the different tested pH conditions. This suggests that the newly designed Pt-Sb alloy electrocatalyst possesses improved charge transfer kinetics relative to the other prepared electrocatalysts. Long-term cycle stability results of the prepared electrocatalysts are displayed in Fig. 5g–i. To compare the stability, the current density (I) of each cycle was normalized by the initial current density (I_0). After 1000 cycles of testing, the $Pt_{5.59}Sb_{4.41}$ electrocatalyst was more stable in acid compared to the Pt electrocatalyst. The Pt and $Pt_{5.59}Sb_{4.41}$ catalysts showed similar catalytic stability in both neutral and base conditions. It seems that the formation of PtSb and $PtSb_2$ alloys in the prepared Pt-Sb electrocatalyst contributes to not only the increased electrochemical glycerol oxidation reactivity but also to improved electrocatalytic stability.

3.5. Product selectivity for EGOR over as-prepared catalysts

To investigate how reaction chemistry for the EGOR changes with the newly developed Pt-Sb hollow structure electrocatalysts in a change of the potential, glycerol concentration, and pH conditions, we conducted experiments using an electrochemical batch reactor system that consists of a three-electrode system with electrocatalysts-coated on titanium (Ti) paper as a working electrode (active area: 2 cm). In Fig. 6 **and** Table S7–S9, the EGOR tests were performed in 0.5 M glycerol dissolved in different electrolytes (acid: 0.5 M H_2SO_4, pH 0.3, neutral: 0.1 M Na_2SO_4, pH 7, and base: 0.1 M KOH, pH 13) for 1 h at 60 ℃ with each different potential. As a result of performing the EGOR test, the major reaction products of Pt were GAD and GLA in acid and neutral conditions. On the other hand, the reaction products of the $Pt_{8.64}Sb_{1.36}$, $Pt_{7.01}Sb_{2.99}$, and $Pt_{5.59}Sb_{4.41}$ electrocatalysts were DHA, GAD, and GLA in acid and neutral conditions (Figs. 6a-6b and Table S7–S8). We found that DHA selectivity increased as the Sb content increased at acid and neutral reaction conditions. In the case of $Pt_{5.59}Sb_{4.41}$, the highest DHA selectivity was observed in both acid and neutral conditions compared to the other tested $Pt_{8.64}Sb_{1.36}$ and $Pt_{7.01}Sb_{2.99}$ catalysts. Interestingly, the DHA selectivity of $Pt_{5.59}Sb_{4.41}$ remained above 80 % regardless of a change of electrode potential in neutral conditions. The DHA selectivity was also up to 89.5 % at a potential of 1.09 V (V *vs.* RHE) under the neutral condition. However, as shown in Fig. 6**c and** Table S9, there was no significant difference in the main products (LA and GLA) under the base condition with all the prepared electrocatalysts. These results suggest that the addition of Sb into Pt significantly changes the reaction chemistry of the EGOR in the acid and neutral conditions and the formation of PtSb and $PtSb_2$ alloys in the prepared Pt-Sb electrocatalyst plays a vital role in the enhancement of DHA selectivity for the EGOR.

To know and compare more detailed changes in reaction chemistry for the EGOR, the product distributions for Pt, $Pt_{8.64}Sb_{1.36}$, $Pt_{7.01}Sb_{2.99}$, and $Pt_{5.59}Sb_{4.41}$ were examined by varying the glycerol concentration (0.1 M, 0.5 M, and 1 M) in different electrolyte solutions as presented in Fig. 7 **and** Table S10–S13. In the acid condition, GAD was the main reaction product by changing the glycerol concentration of 0.1 M, 0.5 M, and 1 M for the Pt electrocatalyst. The GAD selectivity of the Pt catalyst in the acid condition was over 90.0 % at all the glycerol concentrations **(**Fig. 7**a and** Table S10**)** while the $Pt_{5.59}Sb_{4.41}$ electrocatalyst generated DHA as the major product from the change of glycerol concentration (0.1–1 M) in the acidic environment and demonstrated high selectivity of DHA (above ~ 80 %) as presented in Fig. 7**b and** Table S11. The prepared $Pt_{5.59}Sb_{4.41}$ catalyst also maintained high selectivity of DHA (93.3 % in 1 M glycerol) as the glycerol concentration increased from 0.1 M to 1 M. This means that it is possible to selectively produce the valuable DHA chemical at a high glycerol feed concentration for the $Pt_{5.59}Sb_{4.41}$ electrocatalyst. Under neutral conditions, the Pt only catalyst produced GAD as the main product with the different glycerol concentrations similar to the results in acid conditions. Small amounts of DHA and GLA were also generated as byproducts **(**Fig. 7**c and** Table S12**)**. In contrast, the $Pt_{5.59}Sb_{4.41}$ catalyst in the neutral solution exhibited high product selectivity of DHA at the tested glycerol concentrations (0.1– 1 M). The DHA selectivity (94.8 % in 1 M glycerol) tended to increase with the increase of glycerol concentration as shown in Fig. 7**d and** Table S13. More GLA and GAD were made at 0.1 M glycerol concentration compared to the other two glycerol concentrations. Using the Pt and $Pt_{5.59}Sb_{4.41}$ electrocatalysts in the base conditions confirmed that the product distributions of Pt and $Pt_{5.59}Sb_{4.41}$ were similar and the product selectivity of LA for both electrocatalysts

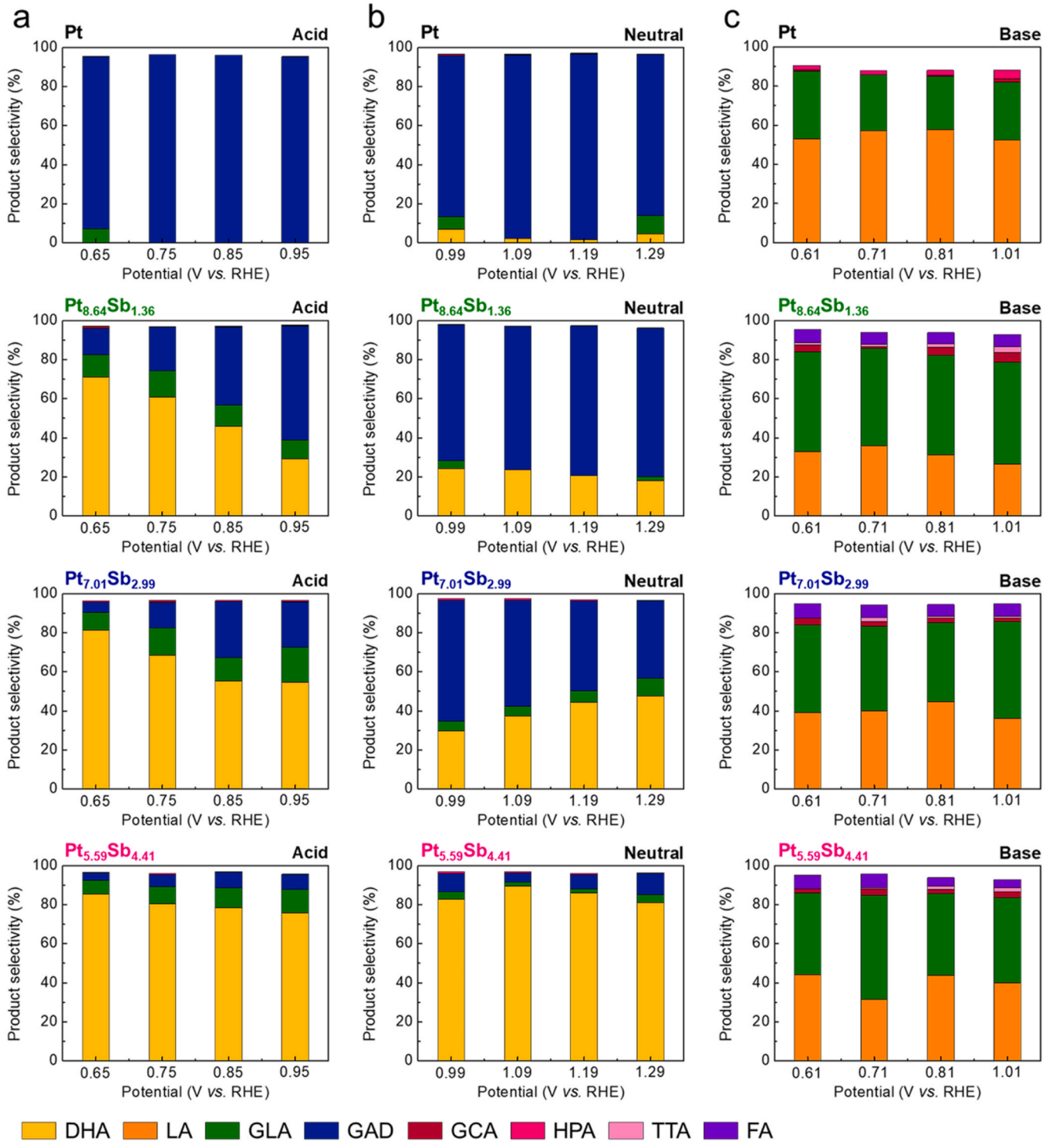

Fig. 6. Reaction chemistry analysis of prepared the Pt, $Pt_{8.64}Sb_{1.36}$, $Pt_{7.01}Sb_{2.99}$ and $Pt_{5.59}Sb_{4.41}$ electrocatalysts for the EGOR at different ph conditions using an electrochemical batch reactor system with the catalysts loaded on titanium (Ti) paper. Investigation and comparison of product selectivity using the prepared electrocatalysts operated at different potentials (V *vs.* RHE) for 1 h in a 0.5 M glycerol solution together with (a) acid (0.5 M H_2SO_4, pH 0.3), (b) neutral (0.1 M Na_2SO_4, pH 7), and (c) base (0.1 M KOH, pH 13).

increased as the concentration of glycerol increased from 0.1 M to 1 M (Fig. S16–S17 **and** Table S14–S15**)**. Small amounts of GCA, HPA, TTA, and FA were also observed as side products. This result indicates that the combinational effect of Pt and Sb in creating PtSb and $PtSb_2$ alloys mainly contributes to a change in the reaction chemistry in the acid and neutral conditions rather than in the base condition. Compared to the product distributions of $Pt_{8.64}Sb_{1.36}$ and $Pt_{7.01}Sb_{2.99}$ electrocatalysts in different glycerol feed concentration solutions, the prepared $Pt_{5.59}Sb_{4.41}$ catalyst demonstrated higher DHA selectivity in the acid and neutral reaction environments and showed reaction results similar to the formation of LA and GLA in the base reaction environment (Fig. S18–S23 **and** Table S16–S21**)**. Therefore, it should be noted that the $Pt_{5.59}Sb_{4.41}$ electrocatalyst with a large portion of PtSb and $PtSb_2$ alloys produces superior DHA selectivity over those of other ratios of Pt-Sb

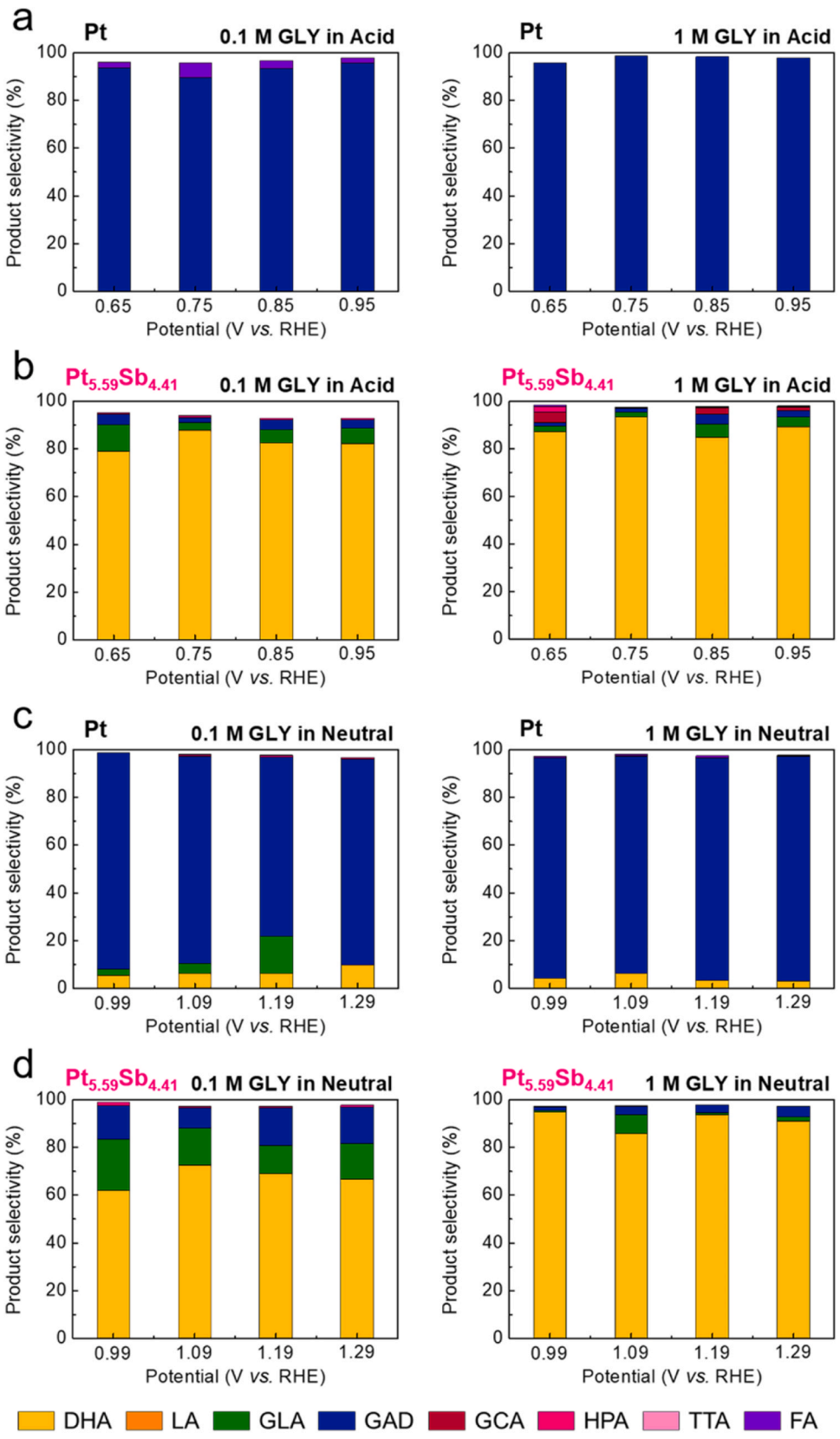

Fig. 7. Selective production of market-valued DHA with the synthesized $Pt_{5.59}Sb_{4.41}$ electrocatalyst for the EGOR in acid (0.5 M H_2SO_4, pH 0.3) and neutral (0.1 M Na_2SO_4, pH 7) conditions. Comparison of product distribution on pt and $Pt_{5.59}Sb_{4.41}$ electrocatalysts operated with different glycerol (GLY) concentrations of 0.1 M and 1 M in acid (a: Pt and b: $Pt_{5.59}Sb_{4.41}$) and neutral (c: Pt and d: $Pt_{5.59}Sb_{4.41}$).

electrocatalysts in acid and neutral conditions, again suggesting the importance of creating the Pt-Sb alloy phases for the selective DHA production from the EGOR. It is also noteworthy that the prepared $Pt_{5.59}Sb_{4.4}$1hollow structure electrocatalyst had the high DHA selectivity at various reaction environments with 0.1–1 M glycerol dissolved in acid and neutral electrolytes compared to other reported catalysts as presented in Table S22. Although some Pt-Sb based catalysts show the high DHA selectivity in acidic conditions including our group's results, the prepared $Pt_{5.59}Sb_{4.41}$ catalyst with PtSb and $PtSb_2$ alloys exhibits high DHA selectivity under the neutral condition and high glycerol concentrations of 0.5 and 1 M, which has rarely been attempted before. To understand and evaluate the reusability of the prepared $Pt_{5.59}Sb_{4.41}$ catalyst electrode in an electrochemical batch reactor for the EGOR, we performed additional experiments in the electrochemical batch reactor, which consisted of a three-electrode system using the larger area electrode (area: 18 cm) of the $Pt_{5.59}Sb_{4.41}$ electrocatalyst loaded on Ti paper as a working electrode (**Fig. S24**). The electrochemical batch reaction tests were conducted more than 30 times using the same $Pt_{5.59}Sb_{4.41}$ catalyst electrode without replacing the electrode in 0.5 M glycerol dissolved in acid and base solutions (**Fig. 8 and Fig. S25**). As presented in Fig. 8, we found that a high DHA selectivity of about 90 % was maintained for 30 times of the batch run testing without replacing the catalyst electrode, indicating the stable catalyst performance of synthesized $Pt_{5.59}Sb_{4.41}$ material for selective DHA production. We additionally investigated the crystal structure of $Pt_{5.59}Sb_{4.41}$ catalyst electrode after the repeated EGOR testing by using the XRD technique. As shown in Fig. S26, the PtSb and $PtSb_2$ alloy phases were still detected, confirming that the crystal structure of $Pt_{5.59}Sb_{4.41}$ catalyst remained stable after the reaction.

3.6. Theoretical investigation

To understand and reveal how the reaction chemistry in the EGOR changes with the prepared Pt-Sb electrocatalysts, density functional theory (DFT) calculations were performed. As shown in Figs. 5–7, the addition of Sb to the Pt catalyst improved both catalytic activity and selectivity for glycerol oxidation. The enhanced catalytic performances were associated with the formation of PtSb and $PtSb_2$ alloys in the synthesized Pt-Sb hollow structure catalysts. To investigate the catalytic effect of Sb in the Pt-Sb electrocatalysts, we computationally analyzed the glycerol oxidation process using the first-principles calculations on three catalytic surfaces: Pt(111), PtSb(100), and $PtSb_2$(111). The catalytic PtSb(100) and $PtSb_2$(111) surfaces were experimentally observed on the $Pt_{5.59}Sb_{4.41}$ sample by the XRD and TEM analyses. We studied the adsorption energies and equilibrium configurations along the reaction pathways for the three catalytic surfaces (**Fig. 9a–d and Fig. S27**). Consistent with previous studies, we observed that two hydroxyl groups of glycerol coordinated to adjacent on-top Pt sites, which stabilized the adsorption of the glycerol molecule on the Pt catalyst[88]. In PtSb, the number of exposed Pt sites was reduced, weakening the Pt–O interaction and making glycerol adsorption less stable. In contrast, surface reconstruction in $PtSb_2$ provided additional spatial flexibility for Pt–glycerol interactions. As a result, $PtSb_2$ exhibited strong glycerol adsorption, comparable to that on Pt. Additionally, strongly adsorbed intermediates were observed on the Pt catalyst. These oxygenated intermediates were known to promote the formation of PtO_x species, which can lead to catalyst deactivation and reduced activity[24]. When Sb was introduced, the same intermediates were loosely bound to the catalysts, thereby reducing poisoning and improving the catalytic activity. For the PtSb and $PtSb_2$ surfaces, Pt–O interaction was weakened compared to the pure Pt surface. Consequently, the Pt–O bond length increased from 2.33 Å on Pt(111) to 2.68 Å on PtSb(100) and 2.74 Å on $PtSb_2$(111). The formation of GAD was thermodynamically preferred on the Pt surface due to the significant energy gap observed between the intermediate and product states in the DHA formation pathway. In contrast to the Pt surface, the PtSb surface exhibited a different behavior. All adsorbed molecules were loosely bound to the PtSb surface. According to the Sabatier principle, such effects can have both positive and negative effects on catalytic activity. However, considering the results in Fig. 5, this trend is likely to have had a positive effect on catalytic activity. Considering that the energy difference between adsorbed glycerol and intermediate states was smaller for the DHA formation pathway than for the GAD formation pathway, we postulated that this step might be the rate-determining step. For the $PtSb_2$ case, DHA was predicted to be preferred over GAD, which is consistent with the experimental results. All the optimized structures are displayed in Fig. S28–S36.

To examine the influence of Sb addition on the electronic structure, we focused on the electrons in the *d* orbitals of Pt atoms and investigated the density of states (DOS) for three catalysts as shown in Figs. 9**e–g**. The DOS of the surface models and the projected density of states (PDOS) at each reaction step are exhibited in Fig. S37–S41. The addition of Sb atoms to the Pt surface showed in a downshift of the *d*-band center of the Pt atom and a narrowing of the *d*-band width. The *d*-band center value of Pt on Pt(111), PtSb(100), and $PtSb_2$(111) in the figures are − 2.33 eV, − 2.97 eV, and − 3.17 eV, respectively. This suggests that the addition of Sb atoms weakened the interaction between adsorbed molecules and catalytic surfaces since downshifted *d*-band center below the Fermi level could imply increased occupation of the Pt–O antibonding state of Pt–O bond (**Fig. S41**) [89–92]. For the case of the PtSb surface, the glycerol adsorption energy becomes closer to zero compared to the pure Pt surface. However, in the case of the $PtSb_2$ surface, surface reconstruction was more predominant than in the other two catalytic surfaces (**Fig. S42**). Due to the surface reconstruction, the glycerol adsorption on the $PtSb_2$ surface became more stable. In addition, as XPS results indicated coexistence of Pt^{2+} and Pt^{4+} cations, we explored the synergistic contribution of both PtSb and $PtSb_2$ phases to the enhanced EGOR performance. To explain the interaction between these phases, we constructed an interface model containing both PtSb and $PtSb_2$ as shown

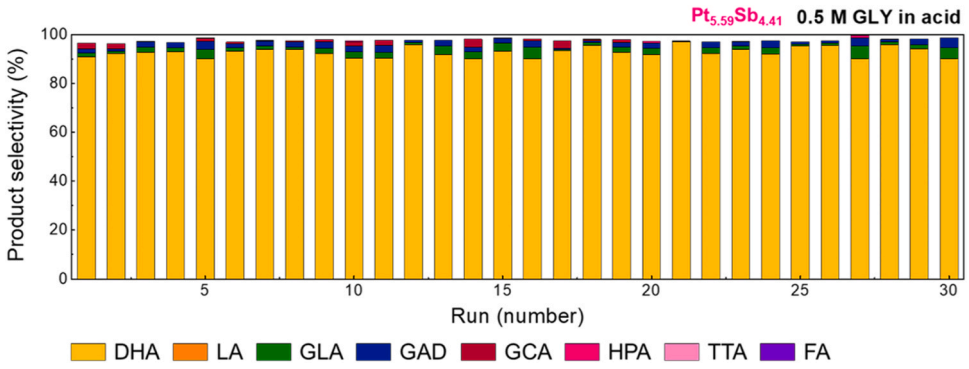

Fig. 8. Product selectivity measurements using a large area electrode (18 cm) with a $Pt_{5.59}Sb_{4.41}$ electrocatalyst during reaction numbers of 30 times at a reaction potential of 0.95 V (V *vs.* RHE) in 0.5 M glycerol solution dissolved in acid.

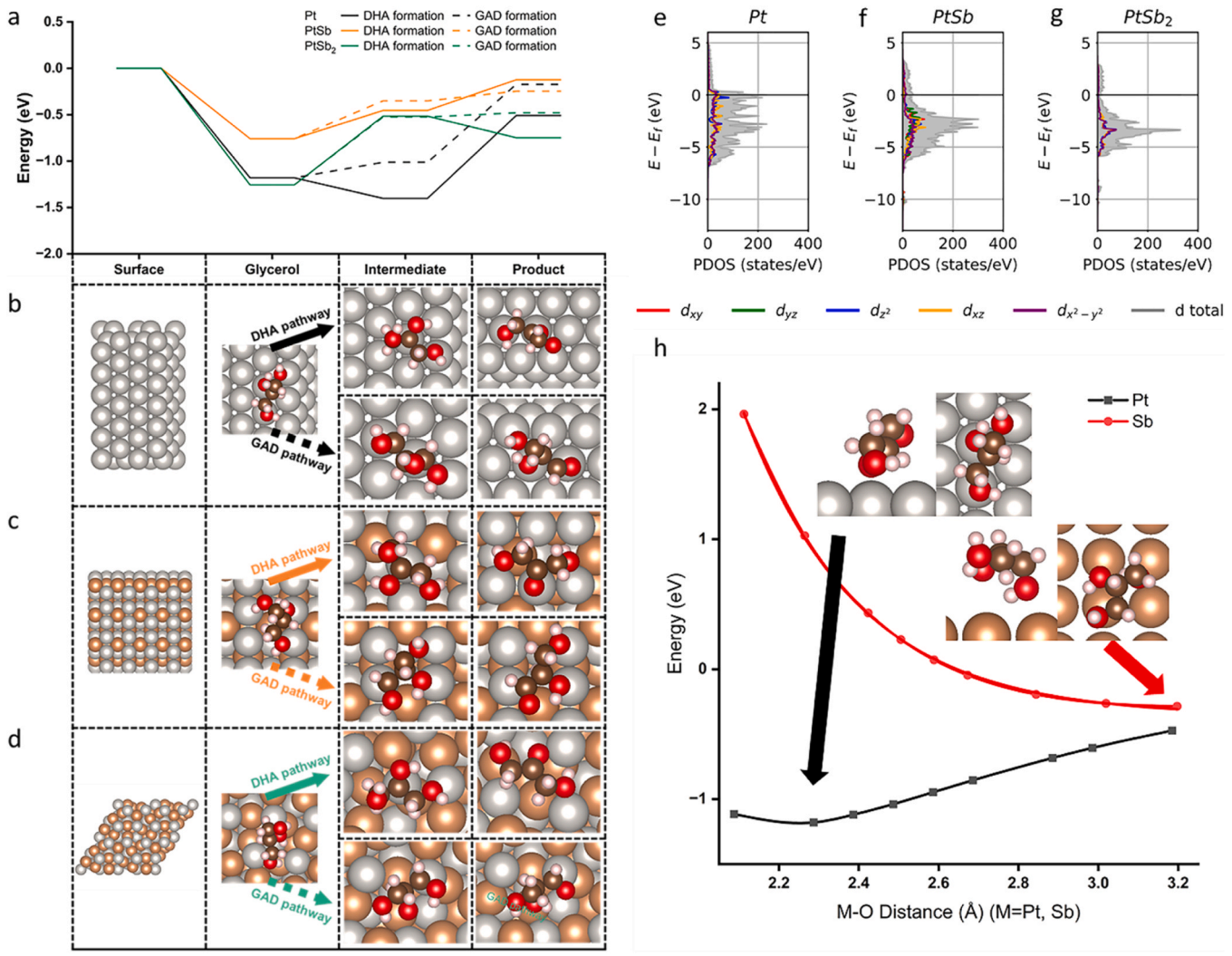

Fig. 9. Computational analysis of the glycerol oxidation process on three different surfaces: Pt(111), PtSb(100), and $PtSb_2$(111). (a) Energy diagram of GAD and DHA formation pathways on Pt, PtSb, and $PtSb_2$. the top view of optimized structures for each step is shown for (b) Pt, (c) PtSb, and (d) $PtSb_2$ surfaces. The projected density of states (PDOS) of pt atom are exhibited for (e) Pt, (f) PtSb, and (g) $PtSb_2$ surfaces. The Fermi energy was set to zero and is represented by a black horizontal line. (h) The adsorption energy curves are presented for the Sb and Pt surfaces with the most stable structures.

in Fig. S43. At the interface between two phases, the intrinsic lattice mismatch caused structural irregularities such as vacancies and stepped surfaces. These irregularities may provide Pt atoms with increased spatial flexibility, enhancing their ability to interact with adsorbates [93]. To investigate the electronic effects, the projected density of states (PDOS) for the Pt *d* orbitals was analyzed. The PDOS analysis showed that the PtSb(100)/$PtSb_2$(111) surface exhibited a downshift in the *d*-band center as shown in Fig. S44. This trend was consistent with that observed for the individual PtSb(100) and $PtSb_2$(111) phases (Fig. 9**f–g**). The inclusion of Sb consistently shifted the *d*-band center further away from the Fermi level compared to Pt(111), indicating a weakened adsorbate–surface interaction. According to the Sabatier principle, such weakening can enhance catalytic performance by optimizing adsorption strength. Based on DFT calculation, we found that the adsorbates preferred to bind to Pt atoms rather than to Sb atoms. Therefore, we investigated the trend of adsorption energy by varying the M-O (M = Pt or Sb) distances between the catalyst and glycerol molecules (Fig. 9**h**). It is clear that the adsorption energies were more stable for the Pt surface than the Sb surface with the shorter Pt-O distance at equilibrium. The computational analysis confirmed that the addition of Sb to Pt catalysts improved the catalytic performance and increased the selectivity of DHA over GAD. In this study, since the Sb atoms did not bind directly to the adsorbates, Pt atoms could be the active sites in all cases. Instead, the Sb atoms modified the electronic property of the Pt atoms and thus modulated the interaction between Pt atoms and adsorbates, which affected both the catalytic performance and the reaction selectivity.

4. Conclusions

In this study, we developed novel Pt-Sb hollow sphere structure electrocatalysts by using a simple one-pot chemical synthesis method. The Pt-Sb hollow catalysts ($Pt_{8.64}Sb_{1.36}$, $Pt_{7.01}Sb_{2.99}$, and $Pt_{5.59}Sb_{4.41}$) synthesized by controlling the Pt:Sb atomic ratio had different catalytic phases, namely, PtSb and $PtSb_2$ alloys. The mixed phases of the PtSb and $PtSb_2$ alloys were formed on the synthesized Pt-Sb catalysts as the Sb content increased in the order of $Pt_{8.64}Sb_{1.36}$, $Pt_{7.01}Sb_{2.99}$, and $Pt_{5.59}Sb_{4.41}$. In particular, more formation of $PtSb_2$ alloy in the $Pt_{5.59}Sb_{4.41}$ catalyst affected the electronic interactions between Pt and Sb orbitals, leading to a Pt *d*-band center shift. The prepared $Pt_{5.59}Sb_{4.41}$ catalyst with PtSb and $PtSb_2$ alloys exhibited excellent EGOR activity among the tested Pt and Pt-Sb electrocatalysts, demonstrating lower onset potential and higher Pt mass activity in the different pH environments (acidic, neutral, and basic). Interestingly, the $Pt_{5.59}Sb_{4.41}$ catalyst material showed high DHA selectivity of about 93.3 % and

94.8 % at a high concentration of 1 M glycerol in acid and neutral conditions, respectively. There was no significant difference in the major products of LA and GLA under a base condition with all the prepared electrocatalysts. This result suggests that the $Pt_{5.59}Sb_{4.41}$ catalyst with PtSb and $PtSb_2$ alloy phases mainly affects the change of reaction chemistry in acid and neutral conditions rather than the base condition. Through theoretical investigations, we obtained a fundamental understanding of the structure-selectivity relation with the created PtSb and $PtSb_2$ alloys at the surface structure of Pt-Sb electrocatalysts. The DFT calculation results confirmed that the formation of DHA is thermodynamically preferred on the Pt-Sb surface sites over the Pt surface site due to the small energy difference observed between the reactant and intermediate states in the DHA formation pathway. In addition, the Sb atoms did not directly interact with adsorbates but instead altered the electronic properties of the Pt atoms and thus modulated the interaction between Pt atoms and adsorbates, which contributed to the enhanced activity and selectivity for the EGOR. In the future work, investigating the optimum ratio between the PtSb and $PtSb_2$ and analyzing the change of EGOR performances at the optimum ratio should be further considered. This study provides critical scientific insights into the design and development of novel electrocatalytic materials for selective production of market-valued chemicals, such as DHA from biomass-derived molecules.

CRediT authorship contribution statement

Hyun Woo Kim: Writing – review & editing, Validation, Software, Data curation. **Hyung Ju Kim:** Writing – review & editing, Supervision, Project administration, Funding acquisition, Formal analysis, Conceptualization. **Ju Ye Kim:** Validation, Investigation. **Youngmin Kim:** Validation, Methodology, Formal analysis. **Jechan Lee:** Methodology, Data curation, Validation, Writing – original draft. **So Hui Jeong:** Validation, Investigation. **Lee Seul Oh:** Writing – original draft, Methodology, Investigation, Formal analysis. **Da Bean Han:** Writing – original draft, Software, Data curation, Validation.

Declaration of Competing Interest

The authors declare that they have no known competing financial interests or personal relationships that could have appeared to influence the work reported in this paper.

Acknowledgements

This work was supported by the core KRICT project [Grant no.: KS2522-20] funded by the Ministry of Science and ICT. This research was also supported by the Ministry of Trade, Industry, and Energy (MOTIE), Korea, under “Innovative Digital Manufacturing Platform” [Grant no.: P0022331] supervised by the Korea Institute for Advancement of Technology (KIAT).

Appendix A. Supporting information

Supplementary data associated with this article can be found in the online version at doi:10.1016/j.apcatb.2025.125591.

Data availability

Data will be made available on request.

References

[1] George W. Huber, Sara Iborra, A. Corma, Synthesis of transportation fuels from biomass: chemistry, catalysts, and engineering, Chem. Rev. 106 (2006) 4044–4098.
[2] M. Simoes, S. Baranton, C. Coutanceau, Electrochemical valorisation of glycerol, ChemSusChem 5 (2012) 2106–2124.
[3] G. Dodekatos, S. Schünemann, H. Tüysüz, Recent advances in thermo-, photo-, and electrocatalytic glycerol oxidation, ACS Catal. 8 (2018) 6301–6333.
[4] Y. Liu, B. Zhang, D. Yan, X. Xiang, Recent advances in the selective oxidation of glycerol to value-added chemicals via photocatalysis/photoelectrocatalysis, Green Chem. 26 (2024) 2505–2524.
[5] C.C. Chong, A. Aqsha, M. Ayoub, M. Sajid, A.Z. Abdullah, S. Yusup, B. Abdullah, A review over the role of catalysts for selective short-chain polyglycerol production from biodiesel derived waste glycerol, Environ. Technol. Innov. 19 (2020).
[6] S.B. Costa-Gutierrez, J.M. Saez, J.D. Aparicio, E.E. Raimondo, C.S. Benimeli, M. A. Polti, Glycerol as a substrate for actinobacteria of biotechnological interest: advantages and perspectives in circular economy systems, Chemosphere 279 (2021) 130505.
[7] M.-H. Jo, J.-H. Ju, S.-Y. Heo, C.-B. Son, K.J. Jeong, B.-R. Oh, Production of high levels of 2,3-butanediol from renewable crude glycerol by klebsiella pneumoniae GEM167 using metabolic engineering and control of oxygen transfer efficiency, Renew. Energy 230 (2024).
[8] S. Lee, H.J. Kim, E.J. Lim, Y. Kim, Y. Noh, G.W. Huber, W.B. Kim, Highly selective transformation of glycerol to dihydroxyacetone without using oxidants by a PtSb/C-catalyzed electrooxidation process, Green Chem. 18 (2016) 2877–2887.
[9] H.J. Kim, Y. Kim, D. Lee, J.-R. Kim, H.-J. Chae, S.-Y. Jeong, B.-S. Kim, J. Lee, G. W. Huber, J. Byun, S. Kim, J. Han, Coproducing value-added chemicals and hydrogen with electrocatalytic glycerol oxidation, Technol. Exp. Techno-Econ. Investig. ACS Sustain. Chem. Eng. 5 (2017) 6626–6634.
[10] J. Han, Y. Kim, D.H.K. Jackson, H. Chang, H.W. Kim, J. Lee, J.-R. Kim, Y. Noh, W. B. Kim, K.-Y. Lee, H.J. Kim, Enhanced catalytic performance and changed reaction chemistry for electrochemical glycerol oxidation by atomic-layer-deposited Pt-nanoparticle catalysts, Appl. Catal. B Environ. 273 (2020).
[11] D. Lee, Y. Kim, H. Han, W.B. Kim, H. Chang, T.-M. Chung, J.H. Han, H.W. Kim, H. J. Kim, Atomic-layer-deposited SnO_2 on Pt/C prevents sintering of pt nanoparticles and affects the reaction chemistry for the electrocatalytic glycerol oxidation reaction, J. Mater. Chem. A 8 (2020) 15992–16005.
[12] Z. He, J. Hwang, Z. Gong, M. Zhou, N. Zhang, X. Kang, J.W. Han, Y. Chen, Promoting biomass electrooxidation via modulating proton and oxygen anion deintercalation in hydroxide, nature, Communications 13 (2022) 3777.
[13] B. Huang, Y. Ge, A. Zhang, S. Zhu, B. Chen, G. Li, Q. Yun, Z. Huang, Z. Shi, X. Zhou, L. Li, X. Wang, G. Wang, Z. Guan, L. Zhai, Q. Luo, Z. Li, S. Lu, Y. Chen, C.S. Lee, Y. Han, M. Shao, H. Zhang, Seeded synthesis of hollow PdSn intermetallic nanomaterials for highly efficient electrocatalytic glycerol oxidation, Adv. Mater. 35 (2023) e2302233.
[14] D. Kim, W.-G. Lim, Y. Kim, L.S. Oh, S. Kim, J.H. Park, C. Jo, H.J. Kim, J. Kang, S. Lee, E. Lim, Amorphous antimony oxide as reaction pathway modulator toward electrocatalytic glycerol oxidation for selective dihydroxyacetone production, Appl. Catal. B Environ. 339 (2023).
[15] L.S. Oh, M. Park, Y.S. Park, Y. Kim, W. Yoon, J. Hwang, E. Lim, J.H. Park, S. M. Choi, M.H. Seo, W.B. Kim, H.J. Kim, How to change the reaction chemistry on nonprecious metal oxide nanostructure materials for electrocatalytic oxidation of biomass-derived glycerol to renewable chemicals, Adv. Mater. 35 (2023) e2203285.
[16] L. Xiong, H. Qi, S. Zhang, L. Zhang, X. Liu, A. Wang, J. Tang, Highly selective transformation of biomass derivatives to valuable chemicals by single-atom photocatalyst ni/TiO_2, Adv. Mater. 35 (2023) e2209646.
[17] L. Wu, Q. Wu, Y. Han, D. Zhang, R. Zhang, N. Song, X. Wu, J. Zeng, P. Yuan, J. Chen, A. Du, K. Huang, X. Yao, Strengthening the synergy between oxygen vacancies in electrocatalysts for efficient glycerol electrooxidation, Adv. Mater. 36 (2024) e2401857.
[18] W. Hong, C. Shang, J. Wang, E. Wang, Bimetallic PdPt nanowire networks with enhanced electrocatalytic activity for ethylene glycol and glycerol oxidation, Energy Environ. Sci. 8 (2015) 2910–2915.
[19] S. Li, J. Lai, R. Luque, G. Xu, Designed multimetallic Pd nanosponges with enhanced electrocatalytic activity for ethylene glycol and glycerol oxidation, Energy Environ. Sci. 9 (2016) 3097–3102.
[20] S. Verma, S. Lu, P.J.A. Kenis, Co-electrolysis of CO_2 and glycerol as a pathway to carbon chemicals with improved technoeconomics due to low electricity consumption, Nat. Energy 4 (2019) 466–474.
[21] S. Li, P. Ma, C. Gao, L. Liu, X. Wang, M. Shakouri, R. Chernikov, K. Wang, D. Liu, R. Ma, J. Wang, Reconstruction-induced NiCu-based catalysts towards paired electrochemical refining, Energy Environ. Sci. 15 (2022) 3004–3014.
[22] S. Wang, Y. Lin, Y. Li, Z. Tian, Y. Wang, Z. Lu, B. Ni, K. Jiang, H. Yu, S. Wang, H. Yin, L. Chen, Nanoscale high-entropy surface engineering promotes selective glycerol electro-oxidation to glycerate at high current density, Nat. Nanotechnol. (2025).
[23] L. Fan, B. Liu, X. Liu, N. Senthilkumar, G. Wang, Z. Wen, Recent progress in electrocatalytic glycerol oxidation, Energy Technol. 9 (2020).
[24] W. Chen, L. Zhang, L. Xu, Y. He, H. Pang, S. Wang, Y. Zou, Pulse potential mediated selectivity for the electrocatalytic oxidation of glycerol to glyceric acid, Nat. Commun. 15 (2024) 2420.
[25] J.F. Gomes, G. Tremiliosi-Filho, Spectroscopic studies of the glycerol electro-oxidation on polycrystalline au and pt surfaces in acidic and alkaline media, Electrocatalysis 2 (2011) 96–105.
[26] Y. Kwon, K.J.P. Schouten, M.T.M. Koper, Mechanism of the catalytic oxidation of glycerol on polycrystalline gold and platinum electrodes, ChemCatChem 3 (2011) 1176–1185.
[27] Y. Kwon, S.J. Raaijman, M.T.M. Koper, Role of peroxide in the catalytic activity of gold for oxidation reactions in aqueous media: an electrochemical study, ChemCatChem 6 (2013) 79–81.

[28] H. Wang, L. Thia, N. Li, X. Ge, Z. Liu, X. Wang, Selective electro-oxidation of glycerol over Au supported on extended poly(4-vinylpyridine) functionalized graphene, Appl. Catal. B Environ. (2015) 25–31.

[29] A.C. Garcia, M.J. Kolb, C. van Nierop y Sanchez, J. Vos, Y.Y. Birdja, Y. Kwon, G. Tremiliosi-Filho, M.T.M. Koper, Strong impact of platinum surface structure on primary and secondary alcohol oxidation during electro-oxidation of glycerol, ACS Catal. 6 (2016) 4491–4500.

[30] C. Dai, L. Sun, H. Liao, B. Khezri, R.D. Webster, A.C. Fisher, Z.J. Xu, Electrochemical production of lactic acid from glycerol oxidation catalyzed by AuPt nanoparticles, J. Catal. 356 (2017) 14–21.

[31] Z. Chen, C. Liu, X. Zhao, H. Yan, J. Li, P. Lyu, Y. Du, S. Xi, K. Chi, X. Chi, H. Xu, X. Li, W. Fu, K. Leng, S.J. Pennycook, S. Wang, K.P. Loh, Promoted glycerol oxidation reaction in an interface-confined hierarchically structured catalyst, Adv. Mater. 31 (2019) e1804763.

[32] T. Li, D.A. Harrington, An overview of glycerol electrooxidation mechanisms on Pt, Pd and Au, ChemSusChem 14 (2021) 1472–1495.

[33] T. Hamada, M. Chiku, E. Higuchi, C.A. Randall, H. Inoue, Effect of silver modification on the kinetics and mechanisms of an electrochemical glycerol oxidation reaction at a platinum electrode in an alkaline medium, ACS Appl. Energy Mater. 7 (2024) 1970–1982.

[34] Y. Li, X. Wei, R. Pan, Y. Wang, J. Luo, L. Li, L. Chen, J. Shi, PtAu alloying-modulated hydroxyl and substrate adsorption for glycerol electrooxidation to C3 products, Energy Environ. Sci. 17 (2024) 4205–4215.

[35] D. Liu, J.C. Liu, W. Cai, J. Ma, H.B. Yang, H. Xiao, J. Li, Y. Xiong, Y. Huang, B. Liu, Selective photoelectrochemical oxidation of glycerol to high value-added dihydroxyacetone, Nat. Commun. 10 (2019) 1779.

[36] L. Luo, W. Chen, S.M. Xu, J. Yang, M. Li, H. Zhou, M. Xu, M. Shao, X. Kong, Z. Li, H. Duan, Selective photoelectrocatalytic glycerol oxidation to dihydroxyacetone via enhanced middle hydroxyl adsorption over a Bi_2O_3-incorporated catalyst, J. Am. Chem. Soc. 144 (2022) 7720–7730.

[37] João R.M. Almeida, Léia C.L. Fávaro, B.F. Quirino, Biodiesel biorefinery: opportunities and challenges for microbial production of fuels and chemicals from glycerol waste, Biotechnol. Biofuels 5 (2012) 1–16.

[38] A.N.T. Tiong, P.Y.Y. Cheonh, W.F. Chua, N. Kolloju, J.M. Ting, J.J. Thian, Valorization of waste glycerol into value-added dihydroxyacetone via microbial fermentation: feasibility study, Chem. Pap. 78 (2024) 5905–5920.

[39] Y. Lu, B.G. Lee, C. Lin, T.K. Liu, Z. Wang, J. Miao, S.H. Oh, K.C. Kim, K. Zhang, J. H. Park, Solar-driven highly selective conversion of glycerol to dihydroxyacetone using surface atom engineered $BiVO_4$ photoanodes, Nat. Commun. 15 (2024) 5475.

[40] Y. Kwon, Y. Birdja, I. Spanos, P. Rodriguez, M.T.M. Koper, Highly selective electro-oxidation of glycerol to dihydroxyacetone on platinum in the presence of bismuth, ACS Catal. 2 (2012) 759–764.

[41] Y. Kwon, T.J.P. Hersbach, M.T.M. Koper, Electro-oxidation of glycerol on platinum modified by adatoms: activity and selectivity effects, Top. Catal. 57 (2014) 1272–1276.

[42] L. Huang, J.-Y. Sun, S.-H. Cao, M. Zhan, Z.-R. Ni, H.-J. Sun, Z. Chen, Z.-Y. Zhou, E. G. Sorte, Y.J. Tong, S.-G. Sun, Combined EC NMR and in situ FTIR spectroscopic studies of glycerol electrooxidation on Pt/C, PtRu/C, and PtRh/C, ACS Catal. 6 (2016) 7686–7695.

[43] A.C. Garcia, Y.Y. Birdja, G. Tremiliosi-Filho, M.T.M. Koper, Glycerol electro-oxidation on bismuth-modified platinum single crystals, J. Catal. 346 (2017) 117–124.

[44] Y. Kim, H.W. Kim, S. Lee, J. Han, D. Lee, J.R. Kim, T.W. Kim, C.U. Kim, S.Y. Jeong, H.J. Chae, B.S. Kim, H. Chang, W.B. Kim, S.M. Choi, H.J. Kim, The role of ruthenium on carbon-supported PtRu catalysts for electrocatalytic glycerol oxidation under acidic conditions, ChemCatChem 9 (2017) 1683–1690.

[45] Y. Zhou, Y. Shen, J. Xi, Seed-mediated synthesis of PtxAuy@Ag electrocatalysts for the selective oxidation of glycerol, Appl. Catal. B Environ. 245 (2019) 604–612.

[46] Y. Zhou, Y. Shen, J. Xi, X. Luo, Selective electro-oxidation of glycerol to dihydroxyacetone by PtAg skeletons, ACS Appl. Mater. Interfaces 11 (2019) 28953–28959.

[47] M.S. Ahmad, S. Singh, C.K. Cheng, H.R. Ong, H. Abdullah, M.R. Khan, S. Wongsakulphasatch, Glycerol electro-oxidation to dihydroxyacetone on phosphorous-doped Pd/CNT nanoparticles in alkaline medium, Catal. Commun. 139 (2020).

[48] C. Liu, M. Hirohara, T. Maekawa, R. Chang, T. Hayashi, C.-Y. Chiang, Selective electro-oxidation of glycerol to dihydroxyacetone by a non-precious electrocatalyst – CuO, Appl. Catal. B Environ. 265 (2020) 118543.

[49] Y. Zhou, Y. Shen, Electro-oxidation of glycerol by tetrametallic platinum-gold–palladium-silver nanoparticles, J. Appl. Electrochem. 51 (2020) 79–86.

[50] X. Huang, Y. Zou, J. Jiang, Electrochemical oxidation of glycerol to dihydroxyacetone in borate buffer: enhancing activity and selectivity by borate–polyol coordination, Chem. ACS Sustain. Chem. Eng. 9 (2021) 14470–14479.

[51] G.-S. Tran, T.-G. Vo, C.-Y. Chiang, Earth-abundant manganese oxide nanoneedle as highly efficient electrocatalyst for selective glycerol electro-oxidation to dihydroxyacetone, J. Catal. 404 (2021) 139–148.

[52] A.M. Verma, L. Laverdure, M.M. Melander, K. Honkala, Mechanistic origins of the ph dependency in Au-catalyzed glycerol electro-oxidation: insight from first-principles calculations, ACS Catal. 12 (2021) 662–675.

[53] M.K. Goetz, M.T. Bender, K.S. Choi, Predictive control of selective secondary alcohol oxidation of glycerol on NiOOH, Nat. Commun. 13 (2022) 5848.

[54] T.-G. Vo, P.-Y. Ho, C.-Y. Chiang, Operando mechanistic studies of selective oxidation of glycerol to dihydroxyacetone over amorphous cobalt oxide, Appl. Catal. B Environ. 300 (2022).

[55] C. Lin, C. Dong, S. Kim, Y. Lu, Y. Wang, Z. Yu, Y. Gu, Z. Gu, D.K. Lee, K. Zhang, J. H. Park, Photo-electrochemical glycerol conversion over a Mie scattering effect enhanced porous $BiVO_4$ photoanode, Adv. Mater. 35 (2023) e2209955.

[56] M. Sheraz Ahmad, K. Hoong Ng, C.-L. Chen, F. Kabir, T. Witoon, T. Yeong Wu, C. Kui cheng, Nitrogen-phosphorous co-doped palladium electrocatalyst for glycerol electro-oxidation reaction (GEOR): an efficient system for mesoxalic acid and dihydroxyacetone production, Fuel 333 (2023).

[57] G.S. Tran, T.G. Vo, C.Y. Chiang, Operando revealing the crystal phase transformation and electrocatalytic activity correlation of MnO_2 toward glycerol electrooxidation, ACS Appl. Mater. Interfaces 15 (2023) 22662–22671.

[58] T.-G. Vo, P.-Y. Tsai, C.-Y. Chiang, Tuning selectivity and activity of the electrochemical glycerol oxidation reaction by manipulating morphology and exposed facet of spinel cobalt oxides, J. Catal. 424 (2023) 64–73.

[59] T. Yang, Y. Shen, Coupling glycerol conversion with hydrogen production using alloyed electrocatalysts, Langmuir 39 (2023) 12855–12864.

[60] G. Kresse, J. Furthmiiller, Efficiency of ab-initio total energy calculations for metals and semiconductors using a plane-wave basis set, Comput. Mater. Sci. 6 (1996) 15–50.

[61] G. Kresse, J. Furthmüller, Efficient iterative schemes for ab initio total-energy calculations using a plane-wave basis set, Phys. Rev. B 54 (1996) 11169–11186.

[62] P. John, Perdew, Burke Kieron, M. Ernzerhof, Generalized gradient approximation made simple, Phys. Rev. Lett. 77 (1996) 3865–3868.

[63] G. Kresse, D. Joubert, From ultrasoft pseudopotentials to the projector augmented-wave method, Phys. Rev. B 59 (1999) 1758–1775.

[64] S. Grimme, J. Antony, S. Ehrlich, H. Krieg, A consistent and accurate ab initio parametrization of density functional dispersion correction (DFT-D) for the 94 elements H-Pu, J. Chem. Phys. 132 (2010) 154104.

[65] V. Wang, N. Xu, J.-C. Liu, G. Tang, W.-T. Geng, VASPKIT: a user-friendly interface facilitating high-throughput computing and analysis using VASP code, Comput. Phys. Commun. (267 () (2021).

[66] K. Mathew, R. Sundararaman, K. Letchworth-Weaver, T.A. Arias, R.G. Hennig, Implicit solvation model for density-functional study of nanocrystal surfaces and reaction pathways, J. Chem. Phys. 140 (2014) 084106.

[67] K. Mathew, V.S.C. Kolluru, S. Mula, S.N. Steinmann, R.G. Hennig, Implicit self-consistent electrolyte model in plane-wave density-functional theory, J. Chem. Phys. 151 (2019) 234101.

[68] S.J. Hoseini, M. Bahrami, G. Askarisarvestani, S.M. Nabavizadeh, H.R. Shahsavari, E. De Giglio, P. Mastrorilli, PtAu thin film as anode electrocatalyst in methanol fuel cell, J. Clust. Sci. 35 (2024) 1731–1742.

[69] X. Xiao, Y. Shang, Y. Bai, H. Miao, X. Lu, K. Lee, J.-P. Ahn, O. Younis, T. Yu, X. Yang, Pt-decorated bimetallic PdRu nanocubes with tailorable surface electronic structures for highly efficient acidic hydrogen evolution reaction, Int. J. Hydrog. Energy 71 (2024) 1026–1033.

[70] R. Nie, D. Liang, L. Shen, J. Gao, P. Chen, Z. Hou, Selective oxidation of glycerol with oxygen in base-free solution over MWCNTs supported PtSb alloy nanoparticles, Appl. Catal. B Environ. 127 (2012) 212–220.

[71] C.Y. Chan, C.H. Chang, H.Y. Tuan, Synthesis of raspberry-like antimony-platinum (SbPt) nanoparticles as highly active electrocatalysts for hydrogen evolution reaction, J. Colloid Interface Sci. 584 (2021) 729–737.

[72] X. Niu, F. Feng, G. Yuan, X. Zhang, Q. Wang, Hollow MFI zeolite supported pt catalysts for highly selective and stable hydrodeoxygenation of guaiacol to cycloalkanes, Nanomaterials 9 (2019).

[73] Q. Wang, B. Mi, J. Zhou, Z. Qin, Z. Chen, H. Wang, Hollow-structure Pt-Ni nanoparticle electrocatalysts for oxygen reduction reaction, Molecules 27 (2022).

[74] R.J. Isaifan, S. Ntais, E.A. Baranova, Particle size effect on catalytic activity of carbon-supported Pt nanoparticles for complete ethylene oxidation, Appl. Catal. A Gen. 464-465 (2013) 87–94.

[75] M.R. Zamanzad Ghavidel, E.B. Easton, Thermally induced changes in the structure and ethanol oxidation activity of $Pt_{0.25}Mn_{0.75}$/C, Appl. Catal. B Environ. (2015) 150–159.

[76] A.L. Wei Ping Zhou,†,‡, Robert Larsen,§, Rich I. Masel,§, Paul S. Bagus,|, Andrzej Wieckowski*, Size effects in electronic and catalytic properties of unsupported palladium nanoparticles in electrooxidation of formic acid, J. Phys. Chem. B 110 (2006) 13393–13398.

[77] J.R. Kitchin, J.K. Norskov, M.A. Barteau, J.G. Chen, Modification of the surface electronic and chemical properties of Pt(111) by subsurface 3d transition metals, J. Chem. Phys. 120 (2004) 10240–10246.

[78] J. Zhang, M.B. Vukmirovic, Y. Xu, M. Mavrikakis, R.R. Adzic, Controlling the catalytic activity of platinum-monolayer electrocatalysts for oxygen reduction with different substrates, Angew. Chem. 117 (2005) 2170–2173.

[79] L.M.C. Pinto, E.R. Silva, R. Caram, G. Tremiliosi-Filho, A.C.D. Ângelo, Preparation and characterization of ordered intermetallic platinum phases for electrocatalytic applications, Intermetallics 16 (2008) 246–254.

[80] S. Wang, F. Yang, S.P. Jiang, S. Chen, X. Wang, Tuning the electrocatalytic activity of Pt nanoparticles on carbon nanotubes via surface functionalization, Electrochem. Commun. 12 (2010) 1646–1649.

[81] H. Gao, S. Liao, Z. Liang, H. Liang, F. Luo, Anodic oxidation of ethanol on core-shell structured Ru@PtPd/C catalyst in alkaline media, J. Power Sources 196 (2011) 6138–6143.

[82] G. Zhang, C. Huang, R. Qin, Z. Shao, D. An, W. Zhang, Y. Wang, Uniform Pd–Pt alloy nanoparticles supported on graphite nanoplatelets with high electrocatalytic activity towards methanol oxidation, J. Mater. Chem. A 3 (2015) 5204–5211.

[83] T. Gong, H. Alghamdi, D. Raciti, A.S. Hall, Improved alkaline hydrogen oxidation on strain-modulated Pt overlayers at ordered intermetallic Pt–Sb cores, ACS Energy Lett. 8 (2022) 685–690.

[84] C. Ye, Z. Wu, W. Liu, Y. Ren, G. Zhang, J.T. Miller, Structure determination of a surface tetragonal Pt_1Sb_1 phase on Pt nanoparticles, Chem. Mater. 30 (2018) 4503–4507.
[85] Y. Hu, H. Zhang, P. Wu, H. Zhang, B. Zhou, C. Cai, Bimetallic Pt-Au nanocatalysts electrochemically deposited on graphene and their electrocatalytic characteristics towards oxygen reduction and methanol oxidation, Phys. Chem. Chem. Phys. 13 (2011) 4083–4094.
[86] T.-W. Chen, J.-X. Kang, D.-F. Zhang, L. Guo, Ultralong PtNi alloy nanowires enabled by the coordination effect with superior ORR durability, RSC Adv. 6 (2016) 71501–71506.
[87] M.F.R. Hanifah, J. Jaafar, M.H.D. Othman, A.F. Ismail, M.A. Rahman, N. Yusof, F. Aziz, N.A.A. Rahman, One-pot synthesis of efficient reduced graphene oxide supported binary Pt-Pd alloy nanoparticles as superior electro-catalyst and its electro-catalytic performance toward methanol electro-oxidation reaction in direct methanol fuel cell, J. Alloy. Compd. 793 (2019) 232–246.
[88] P. Tereshchuk, A.S. Chaves, J.L.F. Da Silva, Glycerol adsorption on platinum surfaces: a density functional theory investigation with van der waals corrections, the, J. Phys. Chem. C 118 (2014) 15251–15259.
[89] Z. Shen, X. Jin, J. Tian, M. Li, Y. Yuan, S. Zhang, S. Fang, X. Fan, W. Xu, H. Lu, J. Lu, H. Zhang, Cation-doped ZnS catalysts for polysulfide conversion in lithium–sulfur batteries, Nat. Catal. 5 (2022) 555–563.
[90] Q. Jing, Z. Mei, X. Sheng, X. Zou, Q. Xu, L. Wang, H. Guo, Tuning the bonding behavior of d-p orbitals to enhance oxygen reduction through push–pull electronic effects, Adv. Funct. Mater. 34 (2023).
[91] Q. Jing, Z. Mei, X. Sheng, X. Zou, Y. Yang, C. Zhang, L. Wang, Y. Sun, L. Duan, H. Guo, 3d orbital electron engineering in oxygen electrocatalyst for zinc-air batteries, Chem. Eng. J. 462 (2023).
[92] L. Wei, W. Yan, Z. Huang, R. Li, Q. Kong, W.-H. Huang, C.-W. Pao, Z. Hu, H. Lin, N. Chen, Y. Xu, H. Geng, X. Huang, Phase and interface engineering of a Ru–Sn nanocatalyst for enhanced alkaline hydrogen oxidation reaction, Energy Environ. Sci. 17 (2024) 5922–5930.
[93] W. Ebmeyer, P.P. Dholabhai, High-throughput prediction of oxygen vacancy defect migration near misfit dislocations in $SrTiO_3/BaZrO_3$ heterostructures, Mater. Adv. 5 (2024) 315–328.